

Far-flung moraines: Exploring the feedback of glacial erosion on the evolution of glacier length

Robert S. Anderson^{a,b,*}, Miriam Dühnforth^{a,c}, William Colgan^d, Leif Anderson^{a,b}

^a INSTAAR, University of Colorado, Boulder, CO 80303, USA

^b Department of Geological Sciences, University of Colorado, Boulder, CO 80303, USA

^c Department of Earth and Environmental Sciences, LMU Munich, 80333 Munich, Germany

^d CIRES, University of Colorado, Boulder, CO 80309, USA

ARTICLE INFO

Article history:

Received 16 February 2012

Received in revised form 25 August 2012

Accepted 28 August 2012

Available online 4 September 2012

Keywords:

Moraine

Alpine landscapes

Glaciers

Flowline model

LGM

Glacial extent

ABSTRACT

Over many glacial cycles, the glacial erosion of alpine valleys can be sufficient to reduce the length of glaciers in the most recent cycles. We document field cases illustrative of this erosional feedback and model the long-term evolution of glacier lengths analytically and numerically. The general feature we target is a moraine deposited well beyond the last glacial maximum (LGM) limit, which we refer to as a “far-flung” moraine. Firstly, we assemble published observations to illustrate that far-flung moraines are documented around the world. The observations suggest that the downvalley distance to such far-flung moraines can exceed the distance to LGM moraines by up to twofold. Secondly, we address the problem analytically, making several simplifying assumptions, to demonstrate that glacier length scales linearly with erosion depth. Finally, we employ a numerical model to test the analytical solution. This 1D (depth-integrated) flowline model includes: (i) a depth-averaged longitudinal coupling stress approximation, (ii) prescribed winter and summer surface mass balance profiles, (iii) evolving ice temperature calculated via the conventional heat equation, and (iv) glacier sliding velocity parameterized as a function of basal ice temperature and spatially and temporally variable prescribed flotation fraction. The simulated alpine landscape is modified through the competing processes of glacier erosion, which is dependent on glacier sliding velocity and prescribed bedrock erodibility, and prescribed uplift rate. The climate controlling surface mass balance is prescribed by time series of air temperature and snowfall approximated by the sum of two sinusoidal cycles. The recurrence statistics of these prescribed climate drivers closely match those of the marine isotopic record; hence the prescribed climate drivers faithfully mimic observed long-term climate drivers.

Consistent with earlier landscape evolution studies, we find that the primary effect of repeated glaciations is to flatten a valley floor and steepen its headwall, effectively cutting a longitudinal notch in a fluvial valley profile. Analytical and numerical model results also demonstrate that far-flung moraines are an inevitable consequence of repeated glaciations: glaciers in tectonically inactive regions can sufficiently erode their valleys so that the earliest glaciations leave moraines many kilometers down-valley from moraines left by the latest glaciations, despite similar climates. This suggests that a different landscape, rather than a different climate, is capable of explaining the early glacier extents. As a corollary, the long-term drift toward reduced glacier length favors the survival of early moraines in the face of later glacial advances. Finally, rock uplift can defeat this erosional feedback, while rock subsidence enhances the feedback.

© 2012 Elsevier B.V. All rights reserved.

1. Introduction

In many alpine settings, the glacial history of the landscape is recorded by a succession of terminal and/or lateral moraines. These

successions, with the oldest terminal moraine being the farthest from the contemporary glacier terminus, provide direct evidence for repeated glaciations over glacial–interglacial timescales. In an attempt to explain the typical number of preserved moraines, Gibbons et al. (1984) suggested that glacier lengths are randomly distributed over time and that after ten glacial cycles, a contemporary moraine succession would most likely contain two to three moraines from past glaciations. We assume that mountain glacier lengths are not driven by a random regional climate but rather broadly follow the benthic $\delta^{18}\text{O}$ record, a proxy for global ice volume. The benthic $\delta^{18}\text{O}$ record (see Fig. 1A) suggests that the Last Glacial Maximum (LGM)

* Corresponding author at: Department of Geological Sciences, University of Colorado, Boulder, CO 80303, USA.

E-mail addresses: robert.s.anderson@colorado.edu (R.S. Anderson), miriam.duhnforth@colorado.edu (M. Dühnforth), william.colgan@colorado.edu (W. Colgan), leif.anderson@colorado.edu (L. Anderson).

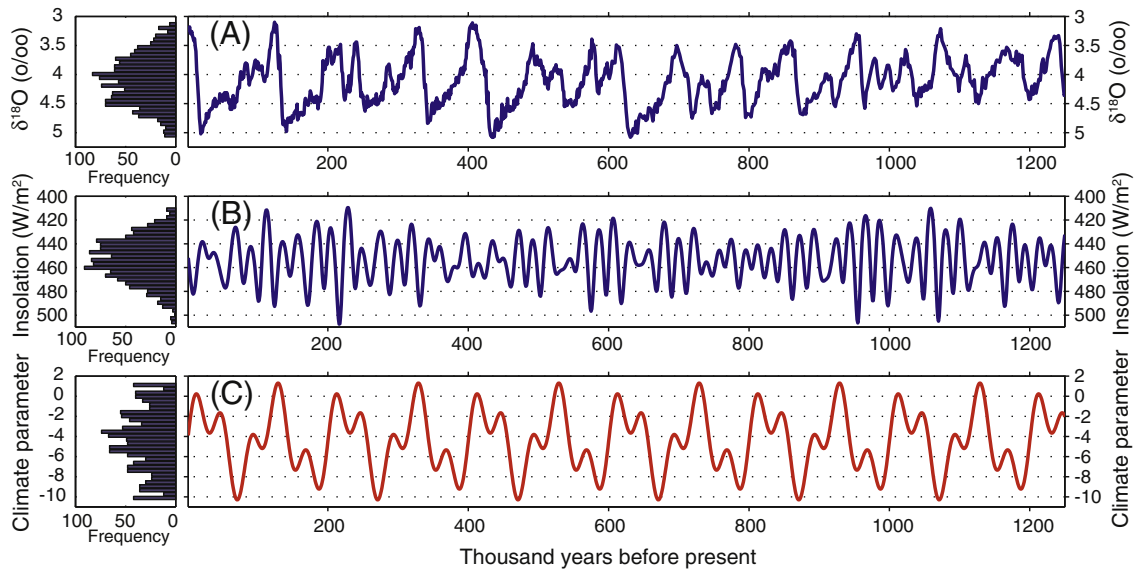


Fig. 1. Time series of potential proxies for climate forcing of glaciers and their histograms. (A) Compilation of benthic oxygen isotope record since the mid-Pleistocene transition (from [Lisiecki and Raymo, 2005](#)). (B) Average June–July–August insolation at 65° N, calculated following [Huybers \(2006\)](#). Both the MIS and insolation records show a strong tendency to occupy the mean state and symmetrical decaying distributions about them. (C) Double sine curve (here of surface air temperature) employed in our glacial model. In this example the chosen periods are 100 and 40 ky, and amplitudes are adjusted so that the peak of the histogram is centered and decays symmetrically toward both highly glacial and highly interglacial conditions.

was as large as any previous glaciation with at least four glacial maxima of similar amplitude ([Lisiecki and Raymo, 2005](#)). If the benthic $\delta^{18}\text{O}$ data does indeed serve as a reliable proxy for the glacier extent in alpine valleys we would – based on the amplitude of the four major past glaciations – expect a succession of terminal moraines that do not show major differences in position. Examples from most major mountain ranges, however, indicate that glacial extents in the past were tens of percent longer than the LGM moraines ([Fig. 2](#)). If we assume that the regional climate driving glaciation in most mountain ranges mimics the global ice volume record, that the LGM was about as large as any previous Plio-Pleistocene glaciation, an alternative explanation is required to explain the preservation of multiple moraines outboard of the LGM moraine ([Table 1](#)).

One alternative explanation for the apparent drift toward reduced glacier length through time is long-term valley profile erosion. [Oerlemans \(1984\)](#) and [MacGregor et al. \(2000\)](#) suggested that long-term erosion of a glacier bed decreases ice-surface elevation and the surface mass balance of a glacier. Glacial erosion has repeatedly been shown to be efficient at modifying alpine landscapes (e.g., [Hallet et al., 1996](#)). Glacial erosion rates, averaged over several time-scales, are typically 1 mm/y. This significantly outpaces fluvial erosion rates, especially in headwaters where river discharge is low. It is therefore reasonable to expect that tens of Quaternary glaciations would result in several hundred meters of valley floor lowering.

[Kaplan et al. \(2009\)](#) echoed this notion. They noted the pattern decreasing glacial extent in Patagonia was not reflected in trends in Southern Hemisphere paleoclimate records and benthic $\delta^{18}\text{O}$, and suggested that the observed pattern could be attributed to long-term glacial erosion and consequent decline in glacier surface mass balance. To our knowledge, while [Singer et al. \(2004\)](#) touch upon the potential role of tectonics in governing the glacial evolution in the Patagonian setting, [Kaplan et al. \(2009\)](#) were the first to explore this erosion – glacier length feedback in a field setting. The complex nature of the Pleistocene Patagonia Ice Sheet, with multiple tributaries and outlet glaciers, and absence of initial bedrock topography, makes their site particularly challenging to simulate in long-term landscape evolution models. In this manuscript, we quantitatively explore the long-term relation between glacier erosion

and glacier length in a characteristic longitudinal valley profile, using idealized initial bedrock topography and climate forcing.

We first employ a simple analytical model to explore the relation between bedrock lowering caused by glacier erosion and glacier length. This exercise demonstrates that the reduction in moraine length is proportional to the mean lowering of the valley floor. We then employ a numerical model that, in contrast to the numerical model used by [Kaplan et al. \(2009\)](#), solves the evolving ice temperature field at discrete time steps and calculates the surface mass balance based on separate summer and winter profiles. This allows us to simulate long-term landscape evolution by glacier erosion, under warm- and cold-based glacier conditions, while honoring seasonal and daily cycles in meltwater production and glacier hydrology. We chose a generic fluvial valley profile as the initial condition to explore the evolution of glacier length in response to glacier erosion. We also explore the influence of tectonic uplift and subsidence by varying uplift and subsidence rates over a plausible range.

2. Assessing a global compilation of far-flung moraines

The succession of terminal moraines described by [Kaplan et al. \(2009\)](#) is not uncommon. [Fig. 2](#) shows that well-documented, far-flung moraines are found in most mountainous regions glaciated during the Plio-Pleistocene.

This diverse population of far-flung moraines was compiled to satisfy the following criteria: (i) paleoglacier lengths could be clearly measured along plausible flow lines from a cirque headwall or modern ice divide to the far-flung moraines; (ii) glacier lengths were only measured for valley glaciers whose far-flung moraines did not extend downstream of a major glacier confluence to eliminate the possibility of glacier coalescence during some glaciations but not others; (iii) Outlet lobes were used in place of far-flung moraines in settings where an ice cap glaciation likely transitioned to a valley glaciation. Numerical moraine ages, or relative moraine age criteria correlated to numerical ages, were available for 87% of cases. The remaining 13% of the moraine ages were inferred from logical marine isotope stage (MIS) assignment based on numerical ages from other moraines within the same valley.

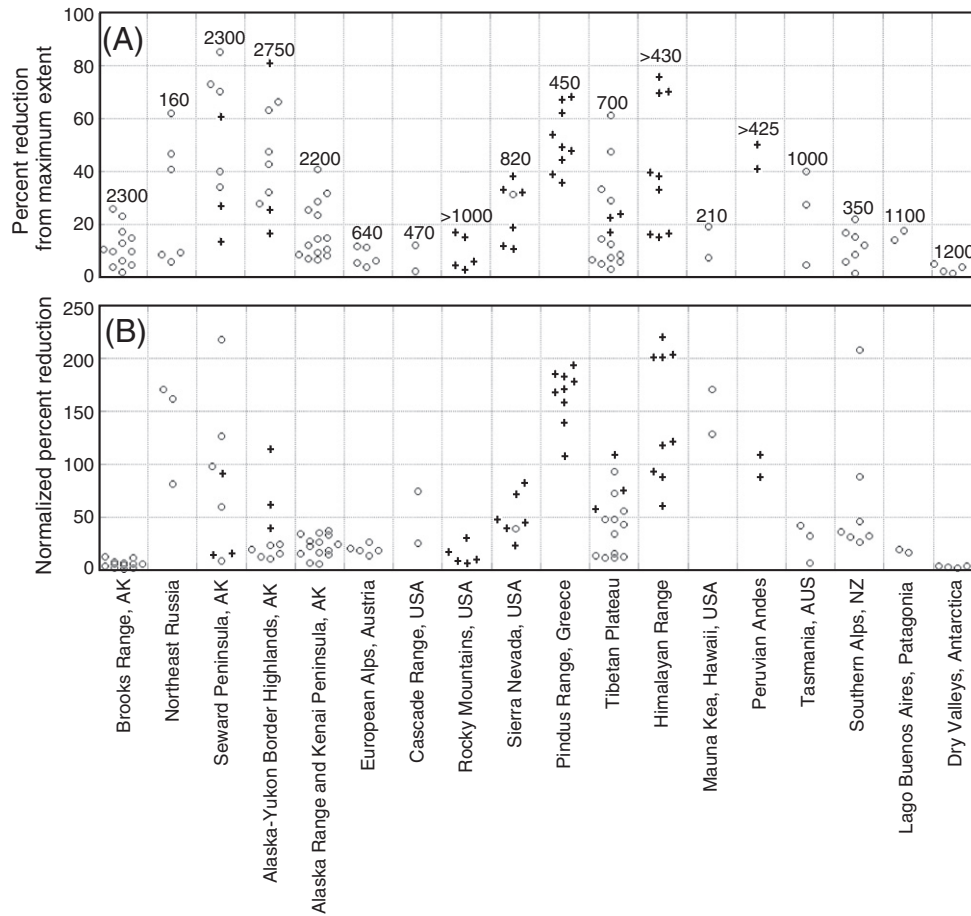


Fig. 2. Global compilation of far-flung moraine observations. Plus markers represent moraines produced by valley glaciers. Circles represent ice cap outlet glaciers. (A) Percent reduction of moraine length relative to the longest documented glacial extent. Dates (in ky) above each column are the oldest moraine age for each region or range. Age from the Cascade Range, USA, is estimated from the LGM moraine counting back MIS stages. (B) Percent reduction in glacial length is normalized to 1 Ma of record (see text for full description). The Northeastern Russia data set also contains data points at 583, 511, and 252% reduction (not plotted). [References: Brooks Range – Hamilton, 1986, 1994; Seward Peninsula – Kaufman and Hopkins, 1986; Alaska-Yukon – Weber and Hamilton, 1982; Weber, 1986; Duk-Rodkin, 1999; Duk-Rodkin et al., 2004; Alaska Range – Kenai Pen. – Schmolli and Yehle, 1986; Kline and Bundtzen, 1986; Thorson, 1986; European Alps – van Husan, 2004; Cascade Range – Porter, 1976; Rocky Mountains – Karlstrom, 2000; Dahms, 2004; Dethier et al., 2003; Sierra Nevada Range – Blackwelder, 1915; Birkeland, 1964; Birman, 1964; Curry, 1971; Sharp, 1972; Pindus Range – Hughes et al., 2006; Tibetan Plateau – Lehmkühl, 1998; Yi et al., 2002; Owen et al., 2005; Colgan et al., 2006; Wang et al., 2007; Xu and Zhou, 2009; Owen et al., 2010; Himalayan Range – Fushimi, 1978; Owen et al., 2006; Hedrick et al., 2011; Mauna Kea – Porter, 1979; Peruvian Andes – Smith et al., 2005; Tasmania – Fitzsimons and Colhoun, 1991; Colhoun and Barrows, 2011; Southern Alps – Suggate, 1990; Lago Buenos Aires – Singer et al., 2004; Kaplan et al., 2005; Dry Valleys – Brook et al., 1993].

In Fig. 2A, we show the percent reduction (R) in glacier length between the greatest glacier extent and any documented glacier extents prior to, or including, the LGM according to:

$$R = 100 \left(\frac{x_{term\ max} - x_{term\ i}}{x_{term\ max}} \right) \quad (1)$$

here $x_{term\ max}$ is glacier length at maximum extent, and $x_{term\ i}$ is the reduced glacier length at a later time.

Comparing the percent reduction of glacier length is difficult without acknowledging that the time interval between moraines varies between sites. We attempt to account for this by assuming that the processes (i.e., trends in climate, erosion, or uplift) resulting in reduced glacier extent vary linearly with time. We therefore normalized R by a common time to allow the direct comparison between moraine sets of different time intervals.

$$R_{norm} = R \left(\frac{t_{norm}}{t_{max} - t_i} \right) \quad (2)$$

where t_{norm} is the time to which we normalize all records (1 My), t_{max} is the numerically constrained age of the most extensive moraine, and t_i is the age of the retracted moraines of interest. The derived R_{norm} values vary widely between mountainous regions. Yet the data

assembled in Fig. 2 suggests that the majority of moraines are within 10 to a few tens of percent of the maximum ice extent. This provides a globally relevant modeling target.

Moraines vary significantly in extent from valley-to-valley and from range-to-range. While we explore the feedback between glacier erosion and glacier length as the global cause of this variability, there are several other potential mechanisms at play at the local or regional scale. These long term mechanisms could include: (i) a decline in available moisture potentially caused by changes in nearby topography, (ii) range-scale rock subsidence, (iii) changes in the underlying lithology that governs both bedrock erodibility and bed roughness, (iv) changes in ice discharge caused by drainage piracy, or (v) significant modification of the glacial valley geometry (i.e., cross-sectional widening by lateral erosion or longitudinal extension by headwall retreat). Many of the extreme R and R_{norm} values in Fig. 2 can be explained by changes in moisture source due to topographic blocking and/or subsidence as described below.

2.1. The potential role of changes in topographic blocking or moisture routing

Late Pliocene to early Pleistocene glacial advances in the Yukon-Tanana highlands were significantly more extensive than late

Table 1
List of symbols.

Symbol	Description and unit of measure
A	Flow law parameter [$\text{Pa}^{-3} \text{s}^{-1}$]
A_b	Drainage area [m^2]
A_{bmax}	Maximum drainage area [m^2]
b	Mean annual surface mass balance [m/y]
b_s	Summer surface mass balance [m/y]
b_w	Winter surface mass balance [m/y]
b_{wmin}	Minimum winter surface mass balance [m/y]
b_{wmax}	Maximum winter surface mass balance [m/y]
c_{snow}	Specific heat capacity of snow [$\text{J}/\text{kg} \text{ } ^\circ\text{C}$]
c_{ice}	Specific heat capacity of ice [$\text{J}/\text{kg} \text{ } ^\circ\text{C}$]
C_o	Initial cold content of snowpack [J/m^2]
ΔC	Change in cold content by melt refreezing [J/m^2]
D	Snow depth [m]
D_e	Snow depth scale over which f_m declines by factor of e [m]
Δx	Horizontal distance increment [m]
Δx_{term}	Change in the position of the terminus [m]
Δz_{acc}	Elevation range of accumulation zone [m]
Δz_e	Change in glacier bed elevation due to erosion [m]
\dot{e}	Glacial erosion rate [m/y]
eff_0	Constant for glacial erosion efficiency []
F	Flotation fraction []
F_{max}	Maximum flotation fraction []
f_m	Positive degree day melt factor [m/PDD]
f_{mi}	Melt factor for ice [m/PDD]
f_{ms}	Melt factor for snow [m/PDD]
g	Acceleration due to gravity [m/s^2]
H	Ice thickness [m]
H_e	Ice thickness scale [m]
k	Bedrock channel erosion coefficient [$\text{m}/\text{y}/\text{m}^{2m}$]
k_s	Constant for rock uplift and erosional efficiency [m^{2m}/y]
L_{ice}	Latent heat of fusion of ice [J/kg]
N	Number of intervals []
m, n_c	Area and slope exponents in bedrock erosion rule []
n	Flow law exponent (taken as 3) []
pH	Exponent governing the sensitivity of sliding to ice thickness []
p	Exponent in valley distance – area relation []
P_a	Period of annual air temperature variation [s]
P_d	Period of daily air temperature variation [s]
Q	Depth-integrated ice discharge at a given node [m^2/y]
Q_d	Deformational heat production [$\text{J}/\text{m}^2/\text{s}$]
Q_{di}	Specific ice discharge due to internal deformation [m^2/y]
Q_{ds}	Specific ice discharge due to basal sliding [m^2/y]
R, R_{norm}	Decrease in glacier length [%]; R normalized []
r	Fraction of melt-related heat retained in snowpack []
S	Slope of glacier bed []
t	Time [s or y]
T_{air}	Calculated air temperature [$^\circ\text{C}$]
\bar{T}_{air}	Mean annual air temperature [$^\circ\text{C}$]
ΔT_{air}	Annual amplitude of the air temperature variation [$^\circ\text{C}$]
ΔT_d	Daily variation in air temperature [$^\circ\text{C}$]
t_i	Age of retracted moraine [y]
T_{ice}	Vertical steady-state ice temperature [y]
t_{max}	Age of most outboard moraines [y]
t_{max_real}	Glacial erosion timescale [y]
t_{norm}	Time (normalized to 1 Ma) [y]
\bar{T}_{ref}	Mean annual air temperature at a reference elevation [$^\circ\text{C}$]
T_s	Air temperature at the glacier surface [$^\circ\text{C}$]
\bar{T}_s	Mean annual air temperature [$^\circ\text{C}$]
ΔT_{sa}	Annual amplitude of air temperature variation [$^\circ\text{C}$]
ΔT_{sd}	Daily amplitude of air temperature variation [$^\circ\text{C}$]
T_{snow}	Temperature of snow [$^\circ\text{C}$]
T_{snow_fall}	Snow temperature at the end of the melt season [$^\circ\text{C}$]
u	Horizontal ice velocity [m/y]
u_s	Basal sliding velocity [m/y]
u_{s^*}	Basal sliding velocity scale [m/y]
U	Rock uplift rate [m]
w	Vertical ice velocity [m/y]
x_0	Downglacier distance to the runoff limit [m]
x_e	Scaled downglacier position of peak flotation [m]
x	Horizontal distance, positive in downstream direction [m]
x_{term}, x_{term}'	Downstream position of maximum and erosion-modified terminus [m]
x_{termi}	Length of glacier in retracted position [m]
x_{max}	Domain length [m]
z	Elevation of initial glacier bed [m]
z'	Elevation of modified glacier bed [m]
z_s	Elevation of ice surface [m]

Table 1 (continued)

Symbol	Description and unit of measure
z_{wmid}	Elevation at which snowfall is midway between b_{wmin} and b_{wmax} [m]
z_{ela}	Equilibrium line altitude (ELA) [m]
z_{max}	Maximum elevation of glacier bed [m]
z_{ref}	Reference elevation [m]
γ_{snow}	Surface mass balance gradient [$\text{m}/\text{y}/\text{m}$] = [1/y]
Γ_{air}	Lapse rate in atmosphere [$^\circ\text{C}/\text{m}$]
κ	Thermal diffusivity of ice [m^2/s]
ρ_{ice}	Density of ice [kg/m^3]
ρ_{snow}	Density of snow [kg/m^3]
σ	Elevation scale over which snowfall changes [m]
τ	Total driving stress [Pa]
$\bar{\tau}_{xx}'$	Depth-averaged longitudinal coupling stress [Pa]
τ_b	Basal shear stress [Pa]
τ_{b^*}	Basal shear stress scale [Pa]
θ	Channel convexity []

Pleistocene advances (Fig. 2). Duk-Rodkin et al. (2004) postulated that early glaciations were more extensive in this area, associated with both an ice free Arctic Ocean and topographically lower coast ranges. Extensive late Pliocene to early Pleistocene glaciation (relative to the LGM extent) in the Brooks Range and Seward Peninsula may also reflect a decline in moisture delivery over the last 2–3 Ma, corresponding to a decrease in sea level (during glacial periods) and potentially an increase in sea ice coverage through the Pleistocene. A similar contraction of recent glacial advances has been observed in northeastern Russia, where the MIS 6 and MIS 4 advances were significantly longer than the MIS 2 advance (Stauch and Gualtieri, 2008). Climate modeling suggests that one potential explanation for this reduction in ice extent is that the Fennoscandian ice sheet (FIS) was significantly larger in MIS 4 than in MIS 2, and subsequently the FIS blocked moisture from reaching northeastern Russia (Krinner et al., 2011). Conversely, the FIS may have played the opposite role during MIS 6, when it is believed that the large 140 ky BP ice sheet caused regional cooling enhancing the effects of orbital forcing, and reducing melt in eastern Russia.

2.2. The roles of bedrock uplift and subsidence

Bedrock uplift in a glaciated region would tend to increase accumulation and increase glacier length. On the contrary, bedrock subsidence would have the opposite effect and should decrease glacier lengths. Constraints on bedrock surface uplift are rare and difficult to acquire. The Yellowstone Hotspot represents a unique example where relative surface uplift can be constrained through geomorphological indicators. Surface uplift of 1–4 mm/y is occurring on the leading edge of the hotspot, while surface subsidence of 1 mm/y is inferred on the trailing edge of the Yellowstone Hotspot (Reilinger, 1985; Pierce and Morgan, 1992; Pierce, 2003; Saunders et al., 2007). Pierce and Morgan (1992) compared the typical percent reduction in glacial length (12–4%) of Rocky Mountain MIS 2 (Pinedale) and MIS 6 (Bull Lake) glacial advances to the corresponding percent reduction of glacier lengths from around the Yellowstone Hotspot. Of 30 glaciers examined on the leading northeast edge of the hotspot, 24 were smaller than the typical ratio of 4%. In 17 valleys the Pinedale glaciers actually overrode the older Bull Lake moraines. In contrast, length ratios of glaciers terminating on the trailing southwest edge of the Yellowstone Hotspot are between 51 and 33% (i.e., LGM moraines are inboard from MIS 6 moraines by several-fold more than the average assembled from the remainder of the Rocky Mountains). These different reductions in glacial length likely reflect the effects of bedrock surface uplift and subsidence on glacier lengths.

The island of Hawaii, which is subsiding at a rate of 2.0 ± 0.5 mm/y in the Mauna Kea region, represents another example of bedrock elevation change influencing glacier length (Porter, 1979). Porter (1979) hypothesized that the significant reduction in moraine distance with age on Mauna Kea was associated with its higher elevation in early

glacial times. Although the long-term pattern of thermal subsidence is interrupted by summit cone building events, this effect fails to interrupt the pattern of reduced glacier length through time.

Classic examples of preserved moraine successions can be found at the base of the Sierra Nevada, California, where Russell (1889), Johnson (1904), and Blackwelder (1929) were the first to report three preserved glacial advances (Sherwin, Tahoe, and Tioga, in order of decreasing age). The two younger advances, Tahoe (MIS 6) and Tioga (MIS 2), have been interpreted as evidence for a slightly more intense glacial climate prior to MIS 2, resulting in a terminal position outboard of the Tioga moraines (Bierman et al., 1991). While the relative difference in locations of the Tahoe and Tioga moraines is only a few tens of meters, significantly older deposits of glacial till from the Sherwin glaciation are preserved at distances of about 3–4 km outboard of the Tahoe/Tioga moraines (Blackwelder, 1931; Sharp, 1972).

Rock Creek, on the east side of the Sierra Nevada (Fig. 3), is one example where old till deposits, at distances of many km downvalley of the LGM and penultimate glacials, have been buried by ~770 ky Bishop tuff and dated as Sherwin in age (>740 ky) (Sharp, 1968; Nishiizumi et al., 1989; Crowley et al., 2007; Phillips et al., 2011). If the downvalley extent of glacial deposits is interpreted as an indicator of glacial climate intensity, this would suggest that mid-Pleistocene climatic conditions produced a far stronger glaciation than those of the MIS 2 (LGM) and MIS 6 penultimate glaciations.

3. Analytical model: inevitable glacier length decline

The long-term reduction of glacier length is inevitable when (i) the rate of glacial erosion outpaces the rate of rock uplift, and (ii) regional climatic conditions remain essentially the same from one glacial maximum to the next. We provide an illustrative example of this process in Fig. 4, in which rock uplift is negligible and the surface mass balance profile $b(z)$ is held steady through all glaciations (i.e., the equilibrium line altitude (ELA) remains constant). In steady state, the terminus of an alpine glacier is located where ice discharge,

$Q(x)$, the downvalley integral of surface mass balance, $\int_0^x b(x)dx$,

returns to zero (e.g., Anderson et al., 2006; see also below). If an alpine landscape does not change between two successive glacial maxima and if the climate, represented by $b(z)$, also remains the same, alpine glaciers should have the same length at both glacial maxima. On the other hand, if a glacier significantly erodes its valley footprint, the longitudinal elevation profile, $z(x)$ – on which the longitudinal surface mass balance profile, $b(x)$, is dependent – will be altered for subsequent glaciations, even if $b(z)$ remains the same. The glacier will occupy a lower elevation and therefore will experience a net decrease in accumulation relative to ablation in subsequent glaciations. The integral of this modified surface mass balance profile, $Q(x)$, will

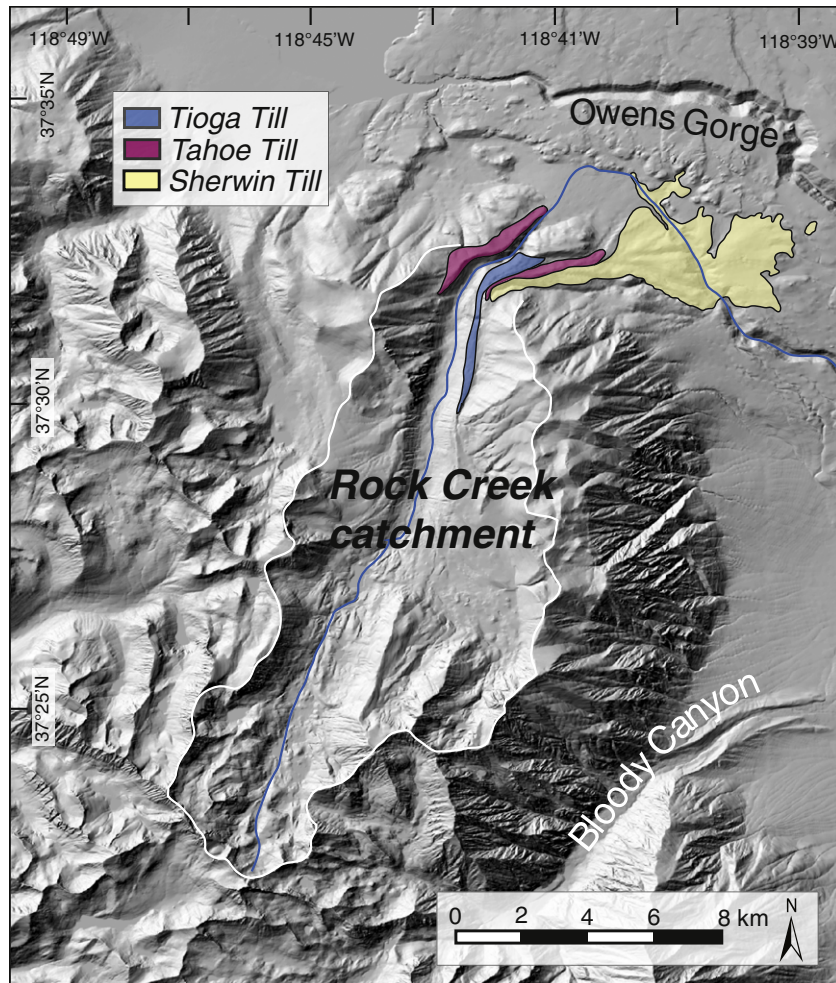


Fig. 3. Hillshade image showing Rock Creek catchment in the eastern Sierra Nevada and the adjacent Owens River Gorge. The maximum extents of mapped glacial deposits from three major glaciations are delineated in yellow (Sherwin; 740 ky), purple (Tahoe; 130 ky), and blue (Tioga; 20 ky). The position of the three deposits suggests that the maximum extent of glaciers decreased by about 6 km from the Sherwin to the Tioga glaciation.

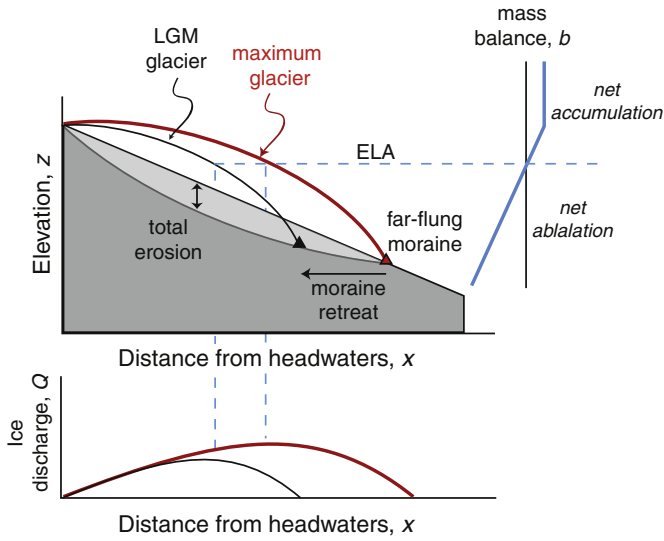


Fig. 4. Valley profiles, $z(x)$, and glacier profiles shown during early and later glacials. Erosion, in a spatial pattern that mimics ice discharge (bottom plot), leads to shorter subsequent glacier length, which promotes the existence of far-flung moraines. Surface mass balance profile $b(z)$ shown at right, with equilibrium line altitude, ELA, separating accumulation zone above from ablation zone below, located where $b=0$. The down-valley integral of the surface mass balance profile is the ice discharge, Q , depicted in the bottom plot for both early and late glacials. In this schematic, we assume no rock uplift and that the surface mass balance profile in early and late glacials is the same.

therefore return to zero at a higher position in the valley in subsequent glaciations (Fig. 4).

We expect the strength of this feedback to depend upon the total erosion that occurs between earliest and latest glacials. A simple illustration of this can be derived by assuming that the spatial pattern of erosion mimics the spatial pattern of ice discharge (e.g., Anderson et al., 2006). For a simple case of a linear initial valley profile, a linear dependence of surface mass balance on elevation results in a parabolic distribution of ice discharge and, hence, erosion (e.g., Fig. 5). When we recalculate the surface mass balance on the eroded profile, $z'(x)$, the new glacier terminus (and accompanying moraine) is indeed closer to the head of the glacier in comparison to the noneroded profile. In Fig. 5 we provide an illustrative example of the fractional reduction in glacier length as a function of total erosion (i.e., cumulative bed incision) for a prescribed valley slope and surface mass balance gradient. This example demonstrates that glacier length can be expected to decrease by several tens of percent for total mean lowering of the bed of one to several hundred meters.

This expectation can be formalized by comparing the analytical expressions for terminus extent in two cases: one with no erosion and the other with uniform erosion. As above, we begin with a linear initial valley profile with prescribed maximum elevation, z_{\max} , and slope, S :

$$z = z_{\max} - Sx. \quad (3)$$

We impose a simple surface mass balance profile that is linear with elevation, with a prescribed equilibrium line altitude, z_{ela} , and surface mass balance gradient, γ :

$$b = \gamma(z - z_{ela}). \quad (4)$$

At steady state, the ice discharge, $Q(x)$, is the downstream integral of surface mass balance:

$$Q = \int_0^x b(x) dx = \int_0^x \gamma((z_{\max} - Sx) - z_{ela}) dx = \gamma(z_{\max} - z_{ela})x - \frac{Sx^2}{2}. \quad (5)$$

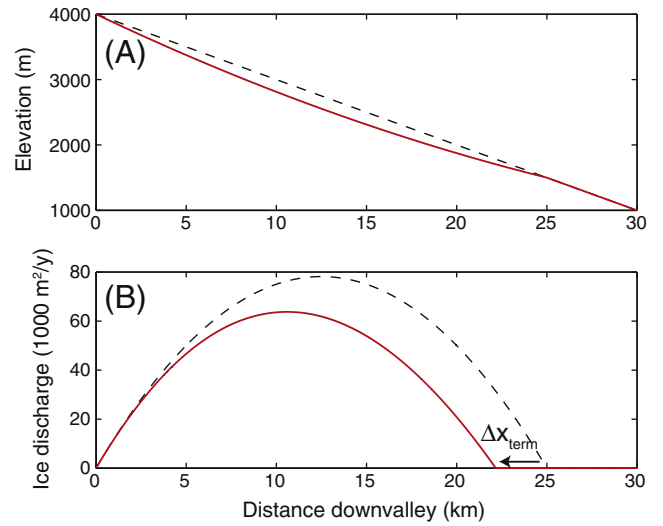


Fig. 5. Simplest model of the erosional feedback over a single erosional episode. Change in valley profile because of glacial erosion (A) and corresponding reduction in glacier length on altered valley profile (B). Initial pattern of ice discharge calculated using the surface mass balance applied to the initial (dashed) profile results in glacier length of 25 km. After erosion (taken to be proportional to the ice discharge), bed elevations and the ice discharge pattern are recalculated (solid red line). The new glacier length, calculated as the location where the discharge goes to zero, is 22 km; the resulting change in terminus position, Δx_{term} , being roughly 3 km.

We evaluate the terminus position (i.e., glacier length) by finding the location in the valley at which the ice discharge returns to zero:

$$x_{term} = \frac{2(z_{\max} - z_{ela})}{S} = \frac{2\Delta z_{acc}}{S} \quad (6)$$

where Δz_{acc} is the elevation range of the accumulation zone. While glacial erosion typically carves an erosional divot that mimics the spatial pattern of ice discharge, for simplicity we instead assume uniform erosion: the valley under the glacier uniformly lowers by Δz_e . The new valley profile is therefore

$$z = z_{\max} - \Delta z_e - Sx. \quad (7)$$

Repeating the calculation of the terminus position reveals

$$x'_{term} = \frac{2(\Delta z_{acc} - \Delta z_e)}{S}. \quad (8)$$

The expected change of terminus position, $x_{term} - x'_{term}$, is proportional to the erosion and inversely proportional to the valley slope:

$$\Delta x_{term} = x_{term} - x'_{term} = \frac{2\Delta z_e}{S}. \quad (9)$$

The fractional change in glacier length is simply

$$\frac{\Delta x_{term}}{x_{term}} = \frac{x_{term} - x'_{term}}{x_{term}} = \frac{\Delta z_e}{\Delta z_{acc}}. \quad (10)$$

The ratio of the final to initial glacier lengths may also be calculated as

$$R = \frac{x'_{term}}{x_{term}} = 1 - \left(\frac{\Delta z_e}{\Delta z_{acc}} \right). \quad (11)$$

The fractional glacier length therefore declines linearly as the ratio of the total erosion (Δz_e) to the original elevation range of the accumulation zone (Δz_{acc}) increases. This closely approximates the results of the illustrative example shown in Fig. 5. Together, these results confirm that erosional lowering of a glacier bed decreases accumulation zone area relative to ablation zone area, which in turn reduces steady state ice discharge to zero at a position that is farther upvalley (see Fig. 6A–C). Notably, this analytical framework can also accommodate the expected changes in glacier length caused by rock uplift ($\Delta z_e < 0$) or subsidence ($\Delta z_e > 0$).

In Fig. 6 we report the results of a simple numerical experiment meant to illustrate the erosional feedback. As in the preceding analytic framework, we assert an unchanging climate characterized by a linear surface mass balance profile $b(z)$. The initial linear valley profile, $z(x)$, is successively eroded by divots that mimic the spatial pattern of ice discharge $Q(x)$ calculated by integrating the surface mass balance profile $b(x)$, and hence $b(x)$, and the resulting ice discharge pattern $Q(x)$. The terminus position, located where ice discharge returns to zero, is plotted in Fig. 6D as

the ratio of glacier length to original length (as in Eq. (11)). The analytic results, assuming uniform erosion, closely approximate the feedback when the surface mass balance is calculated on more complex eroded topography (as long as the erosion used in the scaling is taken to be the mean erosion of the bed). The erosional feedback appears to be potentially significant in that it could account for tens of percent of change in glacier length with plausible amounts of glacial erosion of the valley floor.

While convincing, these first-order analyses have been accomplished by making rather limiting simplifications of the glacial–erosional system. In the following numerical experiments we relax several simplifying assumptions to simulate the interplay between climate, glacier, and landscape evolution. We will find that the results of this analytic treatment are indeed robust.

4. Numerical model: an idealized glacier flowline

In this section we describe the one-dimensional flowline model employed to examine the relation between glacier length and landscape evolution over long timescales. We build upon the models of MacGregor et al. (2000, 2009), Kessler et al. (2006), Dühnforth and Anderson (2011), and Colgan et al. (2012). The finite difference model solves the transient continuity equation for ice, which relates ice thickness change to surface mass balance and the divergence of ice discharge, in combination with the empirical relation between stress and strain rate describing ice rheology. At discrete time steps, we numerically solve the steady-state heat equation and explicitly update parameters dependent on ice temperature. Thus, our model is not fully thermomechanical, as the ice temperature field is not fully transient. Updating the steady-state ice temperature field at discrete time steps, however, provides the computational efficiency required to run multiple 1 My simulations of coupled glacier–landscape evolution.

4.1. Ice flow

The ice flow model solves the transient 1D depth-integrated continuity equation for rate of change in ice thickness ($\partial H/\partial t$):

$$\frac{\partial H}{\partial t} = b_s + b_w - \frac{\partial Q}{\partial x} \quad (12)$$

where b_s and b_w are separately prescribed summer and winter surface mass balances, and $\partial Q/\partial x$ represents the depth-integrated along-flowline divergence of ice discharge (Hooke, 2005). The along-flowline ice discharge at a given node (Q) is calculated as the sum of ice discharge due to sliding ($u_s H$) and deformation according to

$$Q = Q_{side} + Q_{def} = u_s H + \frac{2A}{n+2} \left(\rho_{ice} g \left| \frac{\partial z_s}{\partial x} \right| \right)^{n-1} \tau H^{n+1} \quad (13)$$

where u_s is the calculated basal sliding velocity, A is the temperature-dependent flow law parameter in the empirical relation between stress and strain rate describing ice rheology (Glen, 1955), n is the flow law exponent (taken as 3; Glen, 1958), ρ_{ice} is the density of ice (taken as 917 kg/m³), g is gravitational acceleration (9.81 m/s²), and τ is the total driving stress.

We calculate total driving stress by including depth-averaged longitudinal coupling stress ($\overline{\tau'_{xx}}$) as a perturbation to gravitational driving stress (e.g., Van der Veen, 1987; Marshall et al., 2005):

$$\tau = -\rho_{ice} g H \frac{\partial z_s}{\partial x} + 2 \frac{\partial}{\partial x} \left(H \overline{\tau'_{xx}} \right). \quad (14)$$

Depth-averaged longitudinal coupling stress ($\overline{\tau'_{xx}}$) is calculated following the approach outlined by Van der Veen (1987). This formulation derives longitudinal coupling stress by solving a cubic equation

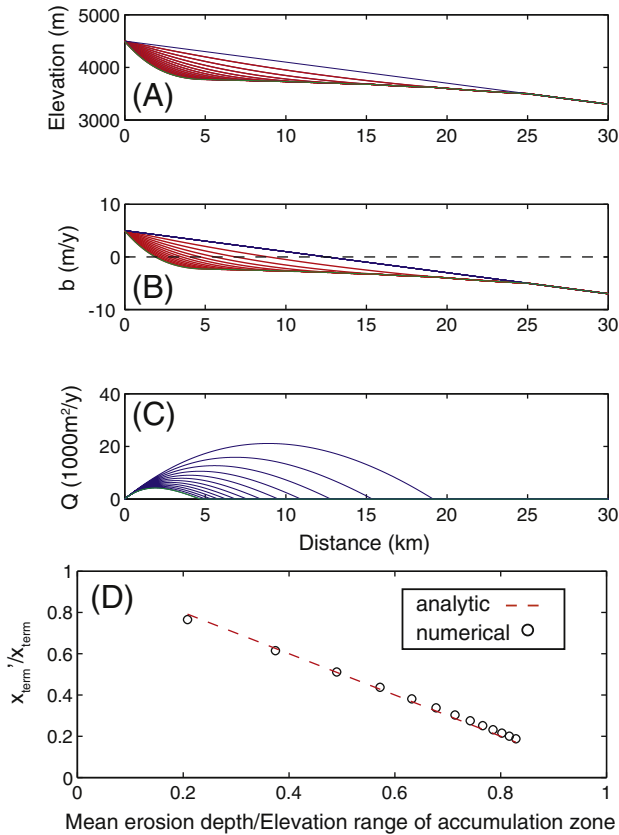


Fig. 6. Simple model illustrating the long-term erosional feedback. (A) Initial valley profile (blue) and successive valley profiles (red) as glacial erosion incises into the initial valley profile. (B) Surface mass balance profiles, $b(x)$, corresponding to the same vertical balance profile, $b(z)$, acting on the successively more eroded valley. The ELA (dashed blue line) intersects the profile at locations progressively farther upvalley. (C) Steady state ice discharge, $Q(x)$, corresponding to the integral of the surface mass balance profile. Terminus locations correspond to where the ice discharge returns to zero. (D) Ratio of terminus position to original position as a function of the mean erosion depth normalized to the elevation range of the accumulation zone. Analytic solution for retreat from uniform lowering of the bed (Eq. (11); red dashed line) captures the essence of the feedback when surface mass balance is calculated on the more complex scoured valley profile. The erosional feedback is capable of reducing glacier length by several tens of percent.

describing equilibrium forces independently at each node, based on ice geometry and prescribed basal sliding velocity (u_s):

$$0 = \bar{\tau}'_{xx} \left\{ 2 \frac{\partial z_s}{\partial x} \left(\frac{\partial H}{\partial x} - \frac{\partial z_s}{\partial x} \right) + H \frac{\partial^2 z_s}{\partial x^2} - \frac{1}{2} \right\} + \bar{\tau}'_{xx} \left\{ \tau \left(\frac{2 \partial H}{3 \partial x} - \frac{3 \partial z_s}{2 \partial x} \right) \right\} \\ + \bar{\tau}'_{xx} \left\{ \tau^2 \left(3 \frac{\partial z_s}{\partial x} \frac{\partial H}{\partial x} + \frac{3}{2} H \frac{\partial^2 z_s}{\partial x^2} - 2 \left(\frac{\partial z_s}{\partial x} \right)^2 - \frac{1}{6} \right) \right\} \\ + \tau^3 \left(\frac{2 \partial H}{5 \partial x} - \frac{1 \partial z_s}{4 \partial x} \right) + \frac{1}{2A} \frac{\partial u_s}{\partial x}. \quad (15)$$

Application of Eqs. (10)–(13) allows the transient form and flow (i.e., geometry and velocity) of a glacier to respond to a prescribed surface mass balance forcing and bedrock topography. These equations were discretized in space using first-order finite control volume methods ($\Delta x = 250$ m). The semidiscrete set of ordinary differential equations was numerically solved using ode15s, the stiff differential equation solver in MATLAB R2008b. Depth-averaged longitudinal coupling stress was explicitly updated every 10 years, while surface mass balance forcing was updated every 40 years, and ice temperature was updated every 100 years. These update frequencies represent the timescales over which each respective variable may be expected to demonstrate significant changes in response to changing ice geometry or climate. A tradeoff exists between update frequency and computational efficiency; increasing update frequency increases the coupling between various model processes, while decreasing update frequency improves computational efficiency.

4.2. Surface mass balance forcing

We employ a climate algorithm with separate winter and summer surface mass balance profiles. Our approach closely follows the method described by Dühnforth and Anderson (2011), and departs from the more complex energy balance algorithms employed, for example, in Anslow et al. (2008). In the winter profile we capture a typical net snowfall accumulation pattern; in the summer profile we capture annually integrated values of both seasonal and daily fluctuations in meltwater production. The winter profile is governed by a pattern of snow accumulation that depends upon elevation, z , such that

$$b_w(z) = b_{wmin} + (b_{wmax} - b_{wmin}) * \tanh[(z - z_w)/\sigma] \quad (16)$$

where b_{wmin} and b_{wmax} are minimum and maximum snowfall (in meters of water equivalent), z_w is the elevation at which the snowfall is precisely halfway between these values, and σ is the elevation scale governing how rapidly the snowfall changes. This formulation honors the observation that snowfall generally increases with elevation until reaching an upper limit (or cap) in many alpine settings. As in MacGregor et al. (2009), we impose an avalanche rule in which snow is removed from headwall slopes exceeding a critical slope, S_c , and is redeposited downvalley in a pattern governed by a decaying exponential with specified length scale λ_{av} .

The summer profile is captured using a positive degree day (PDD) approach to drive meltwater production. Air temperature at the glacier surface is prescribed as a function of annual and diurnal cycles:

$$T_s(z, t) = \bar{T}_s(z) + \Delta T_{sa} \sin(2\pi t/P_a) + \Delta T_{sd} \sin(2\pi t/P_d) \quad (17)$$

where \bar{T}_s is the mean annual air temperature at the surface, taken to vary with elevation through a prescribed environmental lapse rate, Γ_{air} , and a prescribed mean annual air temperature at a reference elevation:

$$\bar{T}_s(z) = \bar{T}_{ref} + \Gamma_{air} (z - z_{ref}) \quad (18)$$

and ΔT and P denote the amplitude and period of the oscillations of annual (subscript a) and diurnal (subscript d) cycles. Annual surface ablation (or snowmelt) is the product of the time-integral (or discrete summation) of air temperatures above the melting point and an assumed PDD melt factor, f_m (e.g., Braithwaite and Olesen, 1989; Ohmura, 2001; Hock, 2003):

$$b_s(z) = f_m \sum \max(0, T_s(z)). \quad (19)$$

To acknowledge that the PDD melt factor, f_m , varies with snowpack albedo, we allow f_m to vary as a function of snow depth by comparing the instantaneous time-integral of snowmelt to total winter snowfall throughout the melt season. We dictate that f_m varies with snow depth through

$$f_m = f_{mi} - (f_{mi} - f_{ms}) e^{-D/D_s}, \quad (20)$$

where D is instantaneous snow depth, f_{ms} is the melt factor for snow, f_{mi} that for ice, and D_s is the snow depth scale over which f_m declines by a factor of e . At any elevation z , the summer surface mass balance then becomes

$$b_s(z) = \sum_{i=1}^N f_m(D) \max(T_s(i), 0) \Delta t \quad (21)$$

where the time interval, Δt , is a small fraction of a day, N is the number of such intervals in a year, $T_s(i)$ is the instantaneous air temperature, and $f_m(D)$ is the snow depth-dependent PDD factor. Thus, both f_m and air temperature vary in space and time.

We employ the calculated meltwater production to determine the temperature of the snowpack remaining at the end of the melt season, as well as the meltwater runoff that enters the englacial and subglacial systems. The snowpack temperature becomes the top boundary condition for the ice temperature model. The cold content of the snowpack is governed by the thickness of the snowpack and the temperature during snowfall (Pfeffer et al., 1991). We take the snowfall temperature to be the mean daily temperature in the middle of the winter (i.e., $\bar{T}_s - \Delta T_{sa}$). The cold content of the snowpack increases with increasing elevation both because snow depth increases with elevation and because the snowfall temperature declines with elevation.

The cold content of the initial snowpack is taken to be

$$C_o = b_w \rho_{snow} c_{snow} (-T_{snowfall}). \quad (22)$$

Cold content is removed by the release of latent heat by meltwater. Melt generated at the snow surface wicks downward in the snowpack until it encounters subfreezing temperatures, at which point it refreezes, thereby releasing latent heat (Pfeffer et al., 1991). The heat generated by refreezing reduces cold content according to

$$\Delta C = b_s \rho_{snow} L_{ice}. \quad (23)$$

The mean snow temperature at the end of the melt season is calculated from the cold content at the end of the melt season:

$$T_{fall} = \frac{(C_o - r \Delta C)}{b \rho_{snow} c_{snow}} \quad (24)$$

where r is the fraction of melt-related heat retained in the snowpack. If melt is sufficient to fill the snowpack pores, pores will connect and allow meltwater to drain from the snowpack above the saturation limit. If the entire pack is warmed to the melting point, water may be released into the englacial and subglacial hydrologic systems. However, as snow is an unsaturated porous substance, it behaves much like a vadose zone, and will only release water if the degree

of saturation is above some threshold. We follow the analysis of Pfeffer et al. (1991), whose research on the Greenland ice sheet suggests that no runoff occurs if the degree of saturation is less than a threshold value of about 70–80%. If a sufficient fraction of the pores in the snow are not filled, they will fail to connect and hence vertical drainage is prevented. We take the retention fraction to be 1.0 (100%) if this condition is not met and 0.7 for all cases in which they connect.

In Fig. 7 we illustrate the resulting winter, summer, and net annual surface mass balance profiles imposed on a synthetic glacier geometry. The ELA in this instance is 3620 m. The snowpack is isothermal below elevations of 4100 m, but the melt is insufficient to fill the pores to the point of drainage above elevations of 3790 m. The expected runoff, which increases monotonically downglacier below this elevation, contributes to subglacial hydrologic processes and feeds river discharge at the terminus.

4.3. Ice temperature field

As significant erosion only occurs beneath warm-based glaciers, and as the flow law parameter (A) is highly dependent on ice temperature (e.g., Hooke, 2005), it is important to model the thermal state of the glacier. We calculate the steady-state vertical profile of ice temperature (T_i) at each node along the flowline using a 2D (cross-sectional) heat equation that captures heat diffusion, advection and production:

$$-\kappa \frac{\partial^2 T_{ice}}{\partial z^2} + u \frac{\partial T_{ice}}{\partial x} + w \frac{\partial T_{ice}}{\partial z} = \frac{Q_d}{\rho_{ice} c_{ice}} \quad (25)$$

where κ is the thermal diffusivity of ice, u and w are ice velocities in the x and z directions, Q_d is deformational (strain) heating, and c_{ice} is the specific heat capacity of ice (Hooke, 2005). We approximate u with the depth-averaged horizontal velocity from the ice flow model, while we use a linear approximation of w from $w = 0$ m/y at the bed to vertical velocity equivalent to the negative of surface mass balance at the ice surface.

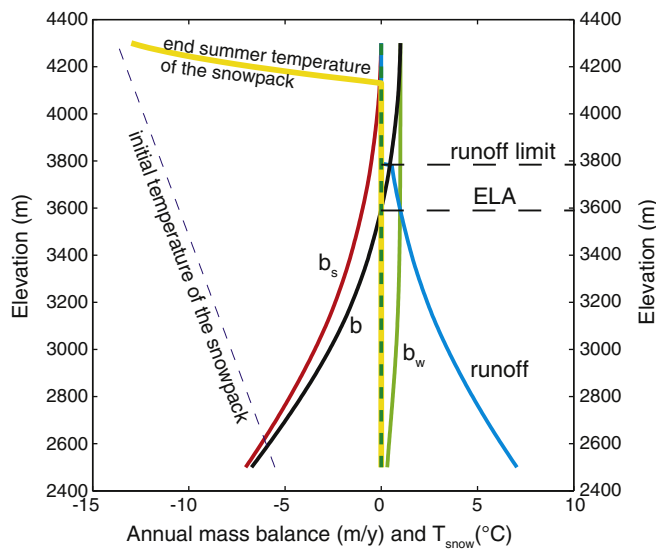


Fig. 7. Surface mass balance profiles for annual winter (b_w), summer (b_s), and net annual mass balance (b) as well as the annual runoff. Snowpack temperature at end of summer (yellow line) and initial temperature of the melt season (blue dashed line) bracket snow temperatures over the course of the melt season. Elevation of the ELA and the runoff limit are indicated by black, dashed lines.

The above heat equation is solved column by column along the flowline, beginning at the glacier head where horizontal velocities are assumed to be negligible (i.e., $u \approx 0$ m/y). This column-by-column solution is facilitated by ignoring horizontal diffusion (i.e., $\partial^2 T / \partial x^2 = 0$), which is typically small compared to horizontal advection. In the accumulation zone, where vertical velocities are downward, calculated ice temperatures that exceed the pressure-melting-point (PMP) are assigned as the PMP, on the assumption that any excess heat is used to melt ice (Funk et al., 1994). In the ablation zone, where vertical velocities are upward, when calculated ice temperatures exceed the PMP the vertical position of the cold-temperate transition surface (CTS) is found through iteration. The iterative solution for the CTS location, above which ice temperature is below the PMP and below which ice is at the pressure-melting-point, satisfies the Clausius–Clapeyron gradient and the upward advection of latent energy by ice with an assumed bulk porosity of 0.01 (Funk et al., 1994).

As most deformation occurs in the bottom 10% of the ice column (Hooke, 2005), we use the calculated ice temperature at 90% depth to update the temperature-dependent flow law parameter in the ice flow model every 100 years.

Numerical solution of the heat equation requires prescribed surface and basal boundary conditions. For the surface boundary condition, we use the mean annual surface ice temperature (T_s) generated by the surface mass balance model (described above). This surface boundary condition, which fluctuates through time in response to periodic forcing of air temperature and accumulation rate, is constrained to remain at or below 0 °C at all times and locations on the glacier. For the basal boundary condition, we prescribe a typical geothermal heat flux of 1 HFU (41 mW/m²).

4.4. Basal sliding rule

The basal sliding velocity of a glacier is dependent upon the driving stress and the state of the hydrologic system. We do not attempt to model the instantaneous hydrologic system of a glacier over 1 Ma. Instead, we parameterize sliding velocity as a function of a mean annual flotation fraction (P_w/P_i)

$$u_s = u_{s^*} F(\tau_b / \tau_{b^*}) (H / H_*)^{pH} \quad (26)$$

where F is the flotation fraction, and u_{s^*} , H_* and τ_{b^*} are characteristic sliding speed, glacier thickness, and basal shear stress scales that allow us to tune the basal sliding speed to known values from glaciers of known thickness and speed. The power to which the ice thickness is raised, pH , governs the sensitivity of sliding to ice thickness. The spatial distribution of the mean annual flotation fraction strongly governs the predicted spatial pattern of sliding. We parameterize the mean spatial pattern of flotation fraction over an annual cycle. At locations above the runoff line, no water is added to the subglacial system from the surface of the glacier (and we assume that the water contributed by off-glacier supraglacial snowmelt, such as that derived from the headwall, is negligible). We attempt to honor the reality of the evolving hydrologic drainage system, as shown in field studies (e.g., Anderson et al., 2004; Bartholomaeus et al., 2007; MacGregor et al., 2009) and as captured in modeling studies (e.g., Kessler and Anderson, 2004; Colgan et al., 2011), with a simple parameterization. Near the terminus, at relatively low elevations, we assume that the existence of an efficient subglacial conduit system prevents the development of high basal water pressures and flotation fraction year-round. Near the headwall, at relatively high elevations, we assume negligible runoff from the upper accumulation zone is available to pressurize the subglacial system year-round. Between these locations, we assume that meltwater production delivers sufficient water to the bed to pressurize the subglacial system and that the absence of efficient conduits for the majority

of the year results in a higher flotation fraction in the middle reach of the glacier. We attempt to capture this mean annual spatial pattern in flotation fraction using a prescribed function of distance downglacier

$$F = F_{\max}(x-x_0)e^{-(x-x_0)/x_*} \quad (27)$$

where F_{\max} is the maximum flotation fraction, x_0 is downglacier distance to the runoff limit (equal to zero when the entire accumulation area generates runoff), and x_* scales the location of the peak flotation (Fig. 8). We have explored other functions, for example a Gaussian distribution centered on the ELA, and find little difference in the final results.

4.5. Erosion rule

We parameterize glacial erosion rate as

$$\dot{e} = \text{eff}_0 * f(\text{sliding}...) \quad (27)$$

where $f(\text{sliding}...)$ is a function of sliding speed, with units of sliding speed, and eff_0 is the vertical erosion rate per unit of sliding speed (and is therefore dimensionless). For example, Humphrey and Raymond (1994) found that $\text{eff}_0 = 10^{-4}$ for the very erodible rock beneath Alaska's Variegated Glacier. While the functional form to be used in this equation is much discussed (e.g., MacGregor et al., 2009), we employ the simplest version in which $f(\text{sliding}...)$ is simply the sliding speed itself, u_s .

4.6. Initial conditions

We employ a generic fluvial valley profile as our initial condition. While loosely based upon western North American alpine ranges, this profile can be shifted in elevation and adjusted in length and relief to capture the essence of fluvial valleys in any mountain range. The profile is derived to honor the essence of fluvial profiles in bedrock channels, which should exist prior to the initiation of a glaciation. A common formulation for the evolution of bedrock river channel elevation is

$$\frac{dz}{dt} = U - kA_b^m S^{n_c} \quad (28)$$

where U is rock uplift rate, A_b is drainage area, S is local channel slope, and k is a local channel erosion efficiency (e.g., Whipple, 2004). We assume that prior to glaciation the profile had achieved a steady-state

shape in which uplift of rock is balanced by erosion. In steady-state, therefore,

$$U = kA_b^m S^{n_c} \quad (29)$$

This results in an analytic solution for the channel slope,

$$S = \left(\frac{U}{k}\right)^{1/n_c} A_b^{-(m/n_c)} = \left(\frac{U}{k}\right)^{1/n_c} A_b^{-\theta} \quad (30)$$

where $1/n_c$ is the channel steepness and θ is the channel convexity. The slope of the channel decreases as the drainage area increases downstream. This may be written equivalently as

$$S = k_s A_b^{-\theta} \quad (31)$$

in which k_s combines the generally poorly known constants of rock uplift rate, U , and erosional efficiency, k (e.g., DiBiase et al., 2010). Once the distribution of drainage area with distance downstream, $A_b(x)$, is known, we may integrate either form of the equation of slope to derive the channel profile. In other words,

$$z = z_{\max} - \int_0^x S(x) dx \quad (32)$$

where the variation in S is entirely governed by the spatial variation in drainage area, A_b . We assume that the drainage area is related through a power law of distance, or

$$A_b = A_{b\max} \left(\frac{x}{x_{\max}}\right)^p \quad (33)$$

and that the existence of a channel requires a critical initial area, A_{\min} . A channel profile $z(x)$ may be generated by specifying the total valley profile length, x_{\max} , the drainage area, A_{\max} , at that location, the elevations z_{\max} at the top of the channel (at $x=0$) and z_{\min} base of the channel (at $x=x_{\max}$), and the parameters of the channel morphology rule, k , m , n_c , and U (or equivalently k_s and θ). We sweep through a range of values for k (or k_s) until we obtain a profile that closely resembles the modern profile of Rock Creek, California, for which the elevation and drainage area are known (Fig. 9). The generic profile we impose as our initial condition is based upon a parameter suite that is similar to that of Rock Creek: an elevation range (i.e., $z_{\max}-z_{\min}$) of 2500 m, a total channel length of 40 km, and a maximum drainage area of 100 km². The values of k_s and θ are derived from the profile in Fig. 9 that best fits the portion of the profile outside of the glacial limit.

4.7. Climate history

We drive our glacial model with a climate history in which we prescribe sinusoidal oscillations in climate. As suggested by Anderson et al. (2006), the marine isotope record indicates that Quaternary climates have been roughly normally distributed: climate is much more likely to have been near the mean Quaternary climate than at either extreme, as pointed out by Porter (1989; Fig. 1). The history of insolation, calculated for 65°N, over the same period also shows a strong preference for the center of its range (Fig. 1B). This feature is not well captured by a single sinusoid, which displays maximum likelihood at the edges of its range. Thus, we use the sum of two sinusoids with different periods to mimic Quaternary climate. When the shorter period sinusoid has approximately half the amplitude of the longer period sinusoid, the highest likelihood climate is indeed identical to the mean of the long period oscillation. We employ time series of climate parameters (i.e., snowfall and air temperature) that display this double sine history, with a ratio of periods of 0.4 (to

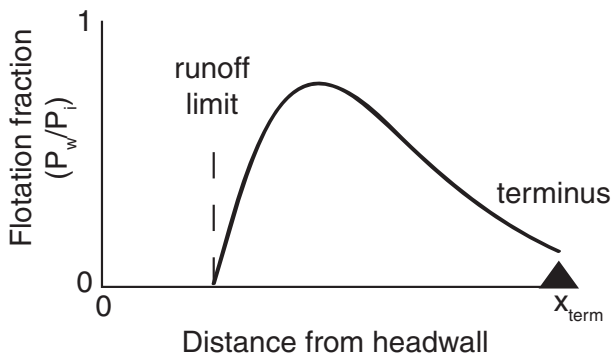


Fig. 8. Down-glacier pattern of mean annual flotation fraction, F , used in the parameterization of basal sliding speed. Runoff occurs only below the runoff limit. Here the spatial pattern of runoff is taken to be a gamma function of distance below the runoff limit.

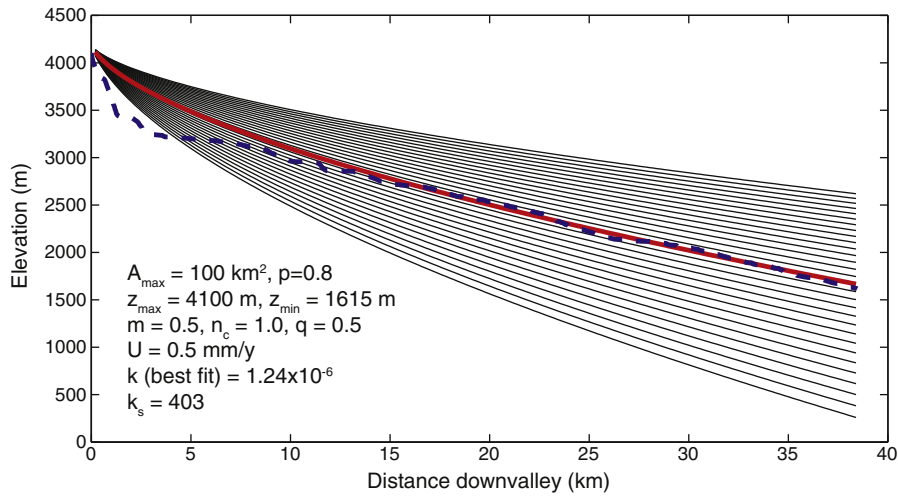


Fig. 9. Calculation of an appropriate initial fluvial profile for Rock Creek, CA. Suite of model profiles corresponding to a range of chosen values for channel erosion efficiency, k . Profile that best fits the profile of Rock Creek, CA, far from its glacial headwaters (distances > 25 km; blue dashed line) is shown in red. The departure of the upper portion of the observed profile from initial fluvial profile suggests a strong influence of glacial erosion.

mimic 40 and 100 ky Milankovitch cycles) and an amplitude ratio of 0.75. This ratio of amplitudes is chosen so that the double sine forcing generates a climate history with a strong central peak in likelihood at the mean climate (Fig. 1C).

4.8. Nondimensional erosion-climate scaling

Glacial valleys have evolved over numerous glacial and interglacial cycles during the Plio-Pleistocene. Prior to the mid-Pleistocene transition (MPT), the dominant climate cycle was 40 ky. Since the MPT, the dominant climate cycle has been 100 ky (e.g., as documented in Lisiecki and Raymo, 2005). As numerical simulations of 100 ky climate cycles are computationally costly – and hence limit our ability to explore the sensitivities of parameter, initial condition and forcing choices – we nondimensionally scale glacier erosion and climate forcing to accelerate the glacial–interglacial cycle. This allows more glaciations to be simulated during a given duration of model time, in comparison to nonscaled simulations. This is similar to the approach of increasing effective time-step (i.e., ratio between real and model time) by nondimensionally scaling ice viscosity in force balance equations (e.g., Bahr and Rundle, 1995). Rather than scaling ice flow, however, we scale climate forcing and landscape response.

In all simulations, we wish to mimic the total valley profile modification that occurs over 1 My. If we execute simulations with 1 model year equal to 1 actual year, we do not need to alter the parameterized erosion rate. If, however, we wish to simulate twice as many glacier – interglacial cycles during an equivalent simulation duration (i.e., enhance effective time-step by two-fold), we should enhance erosion rate by two-fold to generate the corresponding amount of erosion. Thus, assuming that changes in glacier form and flow occur on a far shorter timescale than changes in climate forcing or bed topography (i.e., changes in bed topography or climate are negligible between time steps of the ice flow model), we may explore enhanced computational efficiency by scaling erosion rate and climate forcing period by compensating amounts (i.e., doubling the erosion rate and halving the climate period). To accomplish this, we alter the constant governing efficiency of glacial erosion, eff_0 .

In reality, an erosion efficiency, eff_{0_real} , and a timescale, t_{max_real} , exists over which glacial erosion has shaped a valley profile. We assess whether scaled simulations, in which we reduce the period of climate oscillations and increase erosion efficiency by a corresponding factor, can produce the same final topography and terminus history

as non-scaled simulations. Given a simulation length, t_{max} , the erosion efficiency can be non-dimensionally scaled by

$$eff_0 = eff_{0_real} \left[\frac{t_{max_real}}{t_{max}} \right]. \tag{34}$$

In several simulations, with various erosion rate – climate oscillation scaling, we impose the same history of climate oscillations, but with different periodicity scaling factors (Fig. 10). For the major period, P_1 , we impose $P_1 = t_{max}/10$. In a non-scaled run, in which $t_{max} = t_{max_real} = 1$ My, this major period generates 100-ky cycles to match the eccentricity period. The minor period honors the 4:10 ratio of the 40 ky and 100 ky Milankovitch cycles (i.e., $P_2 = 0.4P_1$).

The resulting glacier length histories are shown in Fig. 10 for several choices of simulation length (t_{max}): 5, 10, 20, 50, and 100 ky. With t_{max_real} equal to 1 My, these runs correspond to non-dimensional scaling factors (i.e., t_{max}/t_{max_real}) of 0.005, 0.01, 0.02, 0.05, and 0.1, respectively. In all runs, we employed $eff_0 = 2 \times 10^{-5}$. In all scaling sensitivity simulations, the histories of climate forcing (air temperature in red, snowfall in blue) perfectly coincide

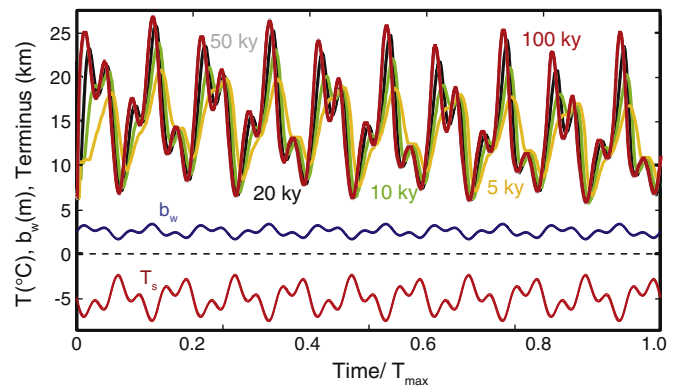


Fig. 10. Variations in glacier length plotted against time normalized by the maximum simulation time. The climate history used for the simulation of the terminus position is controlled by air temperature (lower red line) and snowfall (lower blue line). Note the perfect overlap between the terminus histories of longer simulations (100 and 50 ky; red and gray solid lines) and the obvious departure from this terminus history when the simulations are shorter (5–20 ky; yellow, green, and black solid lines).

when plotted against normalized simulation time. Whereas the 100 ky and 50 ky simulations result in identical terminus histories (the 100 ky model time = 1 My actual time simulation lies directly atop the 50 ky model time simulation), the simulations with shorter duration differ significantly in the amplitude of terminus history. The runs with greater erosion rate – climate forcing scaling also result in different final glacial valley profiles, examples of which are shown in Fig. 11.

We interpret the variation of these sensitivity simulations to reflect variations between the timescales of climate forcing and glacier response time. The shortest of the climate oscillations are $0.4 \cdot 0.1 \cdot t_{max}$ or 4% of t_{max} . For a 10 ky simulation, this is 400 years; while for a 100 ky simulation, this is 4000 years. The response time of glaciers to transient climate can be estimated as the glacier thickness at the ELA divided by the mean negative surface mass balance in the ablation zone (e.g., Jóhannesson et al., 1989). In these simulations, the maximum glacier thickness is ~300 m, and the mean surface ablation rates are ~1 m/y, resulting in expected response times of ~300 years. The effect of this response time is demonstrated by the shortest duration simulations in Fig. 11: the lag between the climate forcing and glacier length becomes evident, and the amplitude of glacier length periodicity is reduced because the climate changes before the glacier reaches dynamic equilibrium. As with the terminus histories, the final bed profiles are virtually indistinguishable for 100 and 50 ky runs, whereas shorter simulations result in different shapes reflecting terminus swings of different amplitude. Thus, the assumption that changes in glacier form and flow occur on a far shorter timescale than changes in climate forcing is invalid for simulations where 1 My of actual time is simulated in <50 ky of model time.

These sensitivity simulations justify the scaling of erosion rate and climate oscillations by an order of magnitude (i.e., 1 My actual time can be simulated in 100 ky of model time) for alpine glaciers with response times of a few hundred years. This honors the separation of timescales between climate forcing and glacier response to transient climate (i.e., $t_{climate} \gg t_{response}$, where $t_{climate}$ is the shortest climate swing and $t_{response}$ is a few hundred years). Thus, we employ $t_{max} = 100$ ky in our non-dimensionally scaled 1 My simulations of glacier – landscape evolution. These simulations can be accomplished in ~1600 processor seconds (as opposed to 16,000 processor seconds for non-scaled simulations).

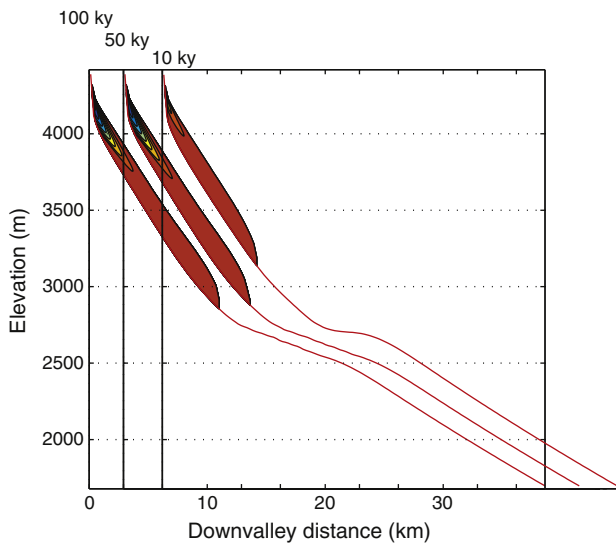


Fig. 11. Longitudinal valley profiles at the end of the 10, 50, and 100 ky simulations. Profiles are offset horizontally to allow comparison. Note the differences in the final glacier lengths and in the morphology of profiles. Colors correspond to internal ice temperatures (see example in Fig. 14 for detail).

5. Results

5.1. Role of surface mass balance and temperature

In Fig. 12 we present our reference simulation. In this simulation, both winter and summer surface mass balances modulate glacier length. No rock uplift is imposed. The glacier length indeed declines as a function of cumulative glacier erosion; the difference between early and late glacial glacier lengths is about 3.5 km, or 18% of the maximum length achieved at 13 ky into the simulation. As shown in Fig. 12B, the analytic solution appears to capture the essence of the erosional feedback. The reduction in glacier length is indeed proportional to the cumulative erosion; the fractional change in glacier length scales with the fraction of the accumulation area elevation range that has been eroded.

In simulations reported in Figs. 13 through 17, we show that the results depicted in the reference simulation are insensitive to climate

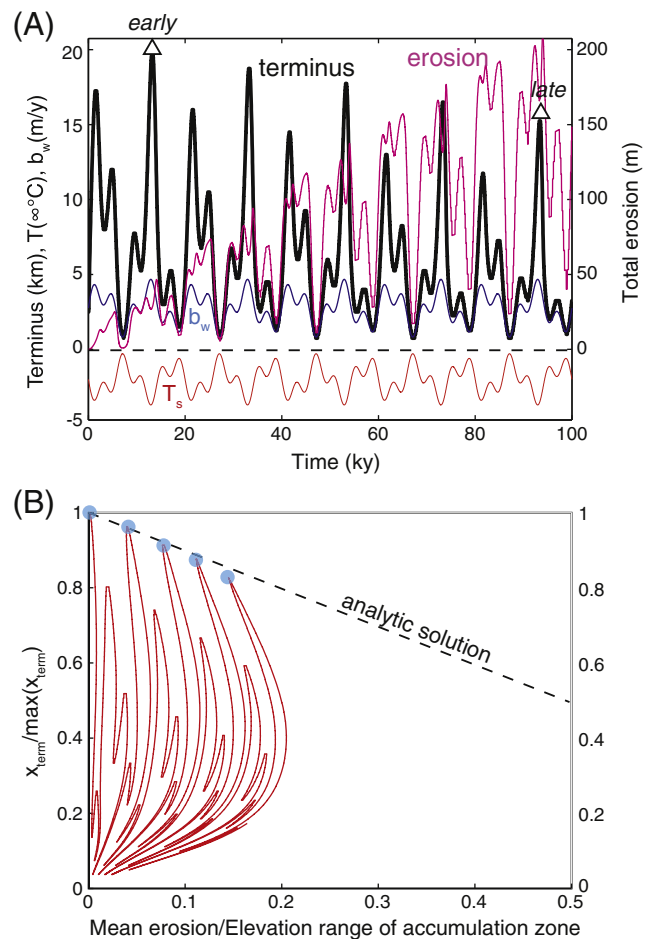


Fig. 12. Co-evolution of glacial landscape and glacier length for a case in which air temperature and snowfall contribute to variability in surface mass balance. (A) Following Fig. 10, time series of meteorological forcing of the glacial system and the corresponding glacier length history. Air temperature ranges from -4 °C to 0 °C while maximum b_w ranges from 0.5 to 5 m/y. The mean erosion beneath the instantaneous glacier is also shown (maroon). As erosion deepens the valley, the glacier length associated with any given climate declines. (B) Assessment of the relation between glacier erosion and terminus position. Blue dots correspond to maximum terminus positions at the peak of major glacials. As in Fig. 5E, we plot the ratio of terminus length normalized against the maximum glacier length, as a function of mean erosion depth beneath the glacier scaled by the elevation age of the accumulation zone, $z_{max-ELA}$ (in this case, 850 m). Here we use the mean ELA calculated over the climate history. Erosion depth is calculated from the time of the peak glaciation (ca. 13 ky) to be consistent with the analytic results. The glacial extents at glacial maxima (blue dots), which should correspond to moraines, decline in a manner that scales linearly with depth of erosion, as the analytic solution (dashed) in Eq. (11) suggests.

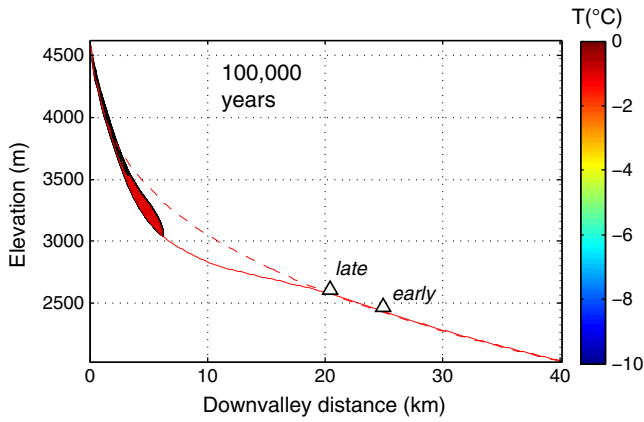


Fig. 13. Glacier valley profiles. Final (solid line) and initial (dashed line) bed profiles bracket the eroded rock volume. T refers to temperature within the ice. Termini associated with early and late glacial cycles are depicted as triangles representing potential moraines. Even at this advanced time slice, surface air temperatures are low enough to promote formation of a cold glacier interior. However, basal ice temperatures are below the PMP only above elevations of ~ 4100 m at this time. Erosion results in ~ 4.5 km reduction in glacier length from the earliest major glacial to the last one.

driver. In Figs. 13–15 the driver is air temperature, so that variability in melt rate dominates variability in glacier length. In this scenario, the air temperatures are low enough during glacials that portions of the basal ice become cold-based, making the glacier polythermal. Basal sliding is disallowed in these portions of the glacier; basal ice temperatures are well below the PMP, as depicted in Fig. 14 at 2 ky into the simulation. In addition, summer surface meltwater production is insufficient to erase the cold content of the snowpack in the upper accumulation area, and less meltwater is available to promote sliding. Both of these effects diminish the amount of basal sliding and hence erosion.

In Figs. 16 and 17 we present the opposite case, in which variation in winter balance (i.e., snowfall) is the dominant climate driver. In this scenario, the basal ice temperatures are never cold enough to curtail sliding, and erosion is therefore greater. Despite the higher mean ELA in this b_w -dominated case (3580 vs. 3440 m), the glacier has eroded more deeply in the same period of time than has the glacier in the air temperature-driven case.

In either case, we see that the strength of the erosional feedback in promoting reduction in glacier length can be explained by the total

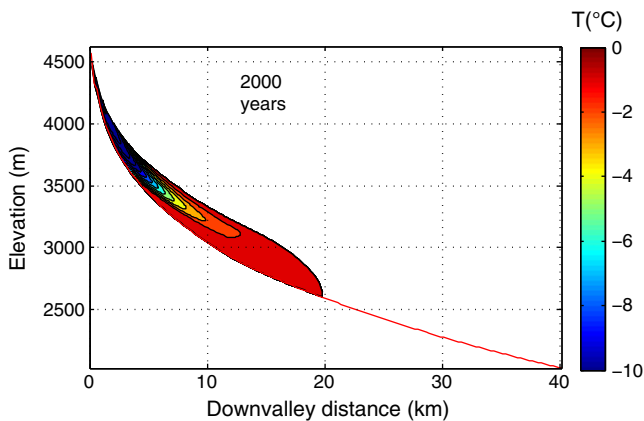


Fig. 14. Early snapshot of simulation shown in Fig. 13. As surface air temperature is so strongly depressed at this time, internal ice temperatures are well below the pressure melting point (PMP). Contours of ice temperature reveal advection of cold ice in the glacier interior, moving downward with the ice in the accumulation zone, and upward below the ELA (at 3200 m in this snapshot), in the ablation zone. Basal ice temperatures above ~ 3700 m are too cold to allow sliding.

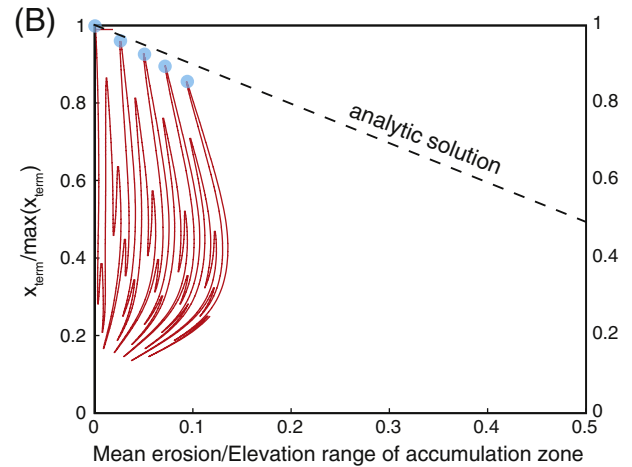
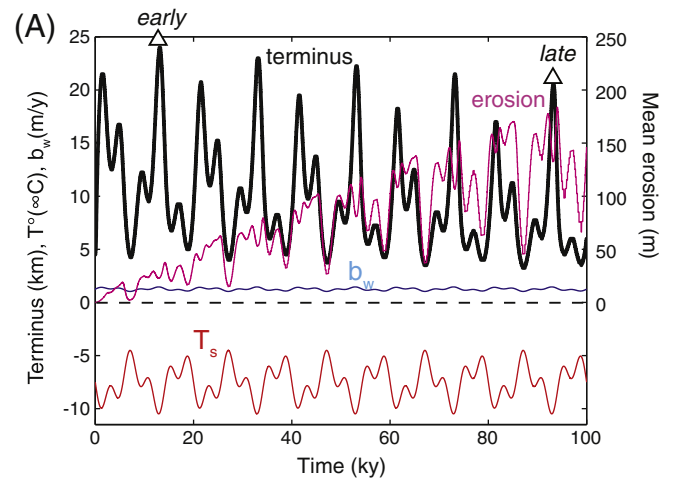


Fig. 15. Co-evolution of glacial landscape and glacier length for air temperature-dominated forcing (0204a case). Details parallel those in Fig. 12. (A) Air temperature ranges from -11 °C to -4 °C, while maximum b_w ranges little, from 1.0 to 1.5 m/y. (B) Ratio of terminus length normalized against the maximum glacier length ($x_{term}/\max(x_{term})$) versus mean erosion/Elevation range of accumulation zone, $z_{max}-ELA$. Here we use the mean ELA calculated over the climate history, 3440 m. The glacial extents at glacial maxima (blue dots), which should correspond to moraines, decline in a manner that scales linearly with depth of erosion, as the analytical solution (dashed) in Eq. (9) suggests. Discrepancy between the analytical and numerical solutions suggests a greater reduction in glacier length can be expected than that suggested by the analytical theory.

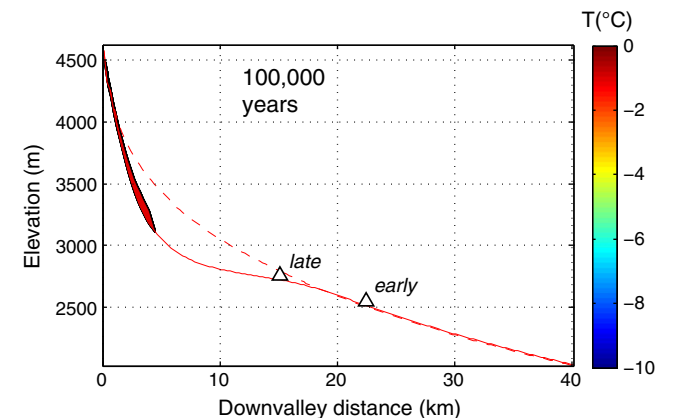


Fig. 16. Glacier valley profiles for case in which winter surface mass balance dominates. See Fig. 13 for description. Significant erosion again results in significant reduction in glacier length through time. The glacier at this point in the glacial cycle occupies only the uppermost steep portion of the valley, and is therefore quite thin.

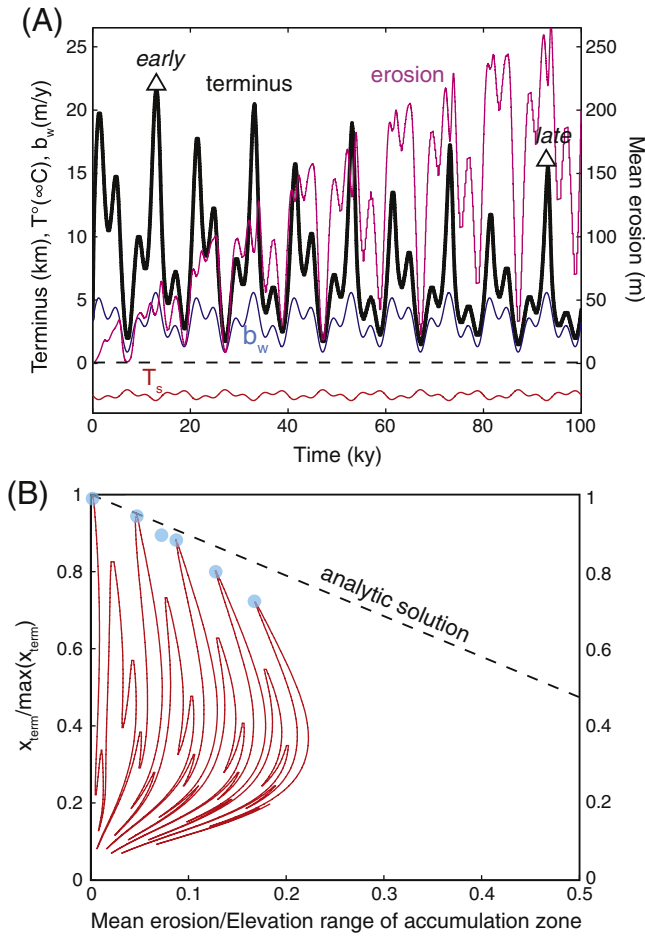


Fig. 17. Co-evolution of glacial landscape and glacier length for snowfall-dominated forcing. See Fig. 12 caption for description. (A) Air temperature ranges little, from -3°C to -2°C , while maximum b_w ranges significantly, from 0.5 to 6.0 m/y. (B) Relation between glacial erosion and terminus position. Mean ELA calculated over the climate history is 3580 m. The glacial extents at glacial maxima (blue dots), which should correspond to moraines, decline in a manner that scales linearly with depth of erosion, as the analytic solution (dashed) in Eq. (9) suggests. Note that total erosion is significantly higher than in the air temperature-dominated case, despite the higher mean ELA. Departure from simple analytic theory is also larger; predicted reduction in glacier length becomes significantly larger than predicted in the analytic solution as erosion deepens.

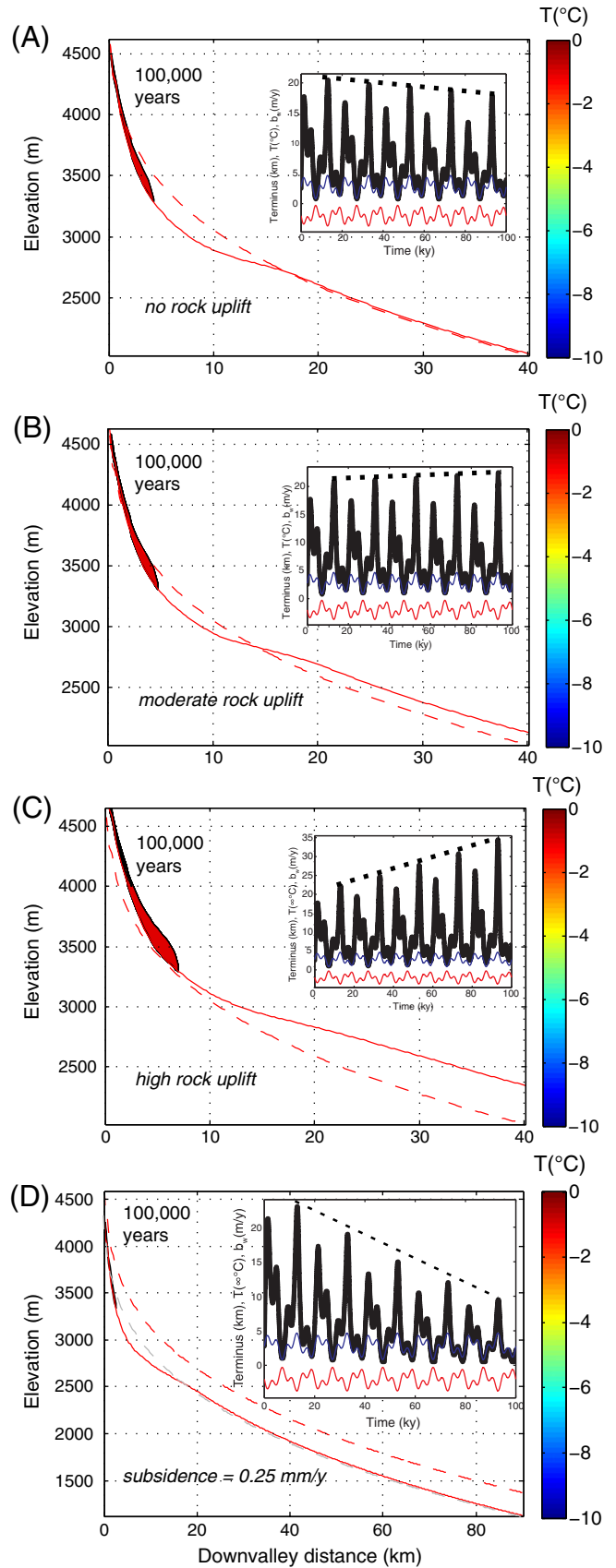
amount of erosion. Glacier length declines roughly linearly with the amount of erosion. If anything, the reduction in glacier length is slightly higher than anticipated using the analytic solution; the analytic solution provides a conservative estimate of the expected reduction in glacier length.

5.2. Role of rock uplift or subsidence

The motion of the rock mass upon which the glaciers are eroding their valleys can either enhance or defeat the glacier erosion–glacier length feedback. As discussed in the introduction, rock uplift can

Fig. 18. Influence of prescribed rock uplift rate on glacier length. Insets mirror Figs. 15A and 17A, depicting time series of meteorological forcing, and terminus position (black bold). (A) No prescribed rock uplift or subsidence. Glacier length declines by $\sim 15\%$ over the course of the simulation (dotted line in inset). (B) Moderate rock uplift = 0.1 mm/y. The erosional feedback is countered, and the glacier extends slightly farther downvalley in each successive glaciation. (C) Significant rock uplift = 0.3 mm/y. Older moraines are over-ridden by younger moraines. (D) Subsidence of 0.25 mm/y is sufficient to enhance significantly the erosional feedback, leading to a wide span of moraine lengths and high likelihood of preservation of all moraines in a glacial sequence.

potentially counter the effect of erosion entirely (e.g., the leading edge of the Yellowstone Hotspot), while subsidence can lead to enhanced reduction in glacial length through time (e.g., Mauna Kea, Hawaii). In Fig. 18A we show a case in which rock uplift is allowed to



result only from isostatic response to the erosion of the valley. As this is minor, the erosional feedback results in roughly a 10% reduction in glacier length, as in our prior simulations. However, if the rock mass is allowed to rise as a block (i.e., in excess of isostatic response; Fig. 18B, C), the erosional feedback is defeated. In case B, the prescribed rock uplift of 0.1 mm/y nearly balances the erosion, and at all glacial maxima the glacier achieves roughly the same length. This could lead to the stacking of moraines into a moraine complex. In case C, the prescribed rock uplift of 0.3 mm/y is sufficient to counteract the erosion feedback altogether, leading to a trend of greatly increasing moraine distances through time. In this instance, no older moraines would be found, and LGM moraines could in fact override MIS 6 moraines, as observed around the Yellowstone Hotspot (Pierce and Morgan, 1992).

If, on the other hand, rock subsidence occurs instead of uplift (Fig. 18D), the sequence of glacier lengths declines more rapidly than in the no-uplift case. In this simulation, the subsidence rate imposed is 0.25 mm/y. At special sites where persistent local subsidence has occurred over the Quaternary, ancient moraines will be truly far-flung, and the sequence will likely be more complete than in locations without subsidence. This supports Porter's (1979) explanation of the Hawaiian Muana Kea moraine set and Pierce and Morgan's (1992) explanation of moraines on the trailing edge of the Yellowstone Hotspot.

6. Discussion

Our numerical investigations demonstrate that glacial erosion and/or rock uplift/subsidence are major controls on the preservation of moraine successions. In contrast to studies that emphasize the role of glaciers as filters of short-term stochastic climate variation (Roe and O'Neal, 2009; Roe, 2011) or that address the number of preserved moraines to be expected over the Plio-Pleistocene (Gibbons et al., 1984), we show that over long timescales glacial erosion crucially controls the history of valley glacier lengths. Our results demonstrate that the erosional feedback scales linearly with the depth of glacial erosion. As implemented, the feedback is insensitive to the details of the prescribed surface mass balance and to the imposed erosion rule. Thus, as a glacial valley erodes downward, subsequent glacial maximum surface elevations are lowered: accumulation is reduced and ablation is increased. This reduction in ice surface elevation through time progressively reduces the health of younger glaciers.

We addressed the role of vertical glacial erosion on Plio-Pleistocene glacial length evolution. Other effects, however, may play important roles. We did not address valley widening or valley headwall retreat (e.g., Brocklehurst and Whipple, 2002; MacGregor et al., 2009). We also ignored any lithologic influence on erosion that could lead to spatial variation in vertical erosion. Our results are therefore only strictly valid for glacial valleys with uniform erodibility. Exploration of the sign and magnitude of these effects (i.e., geometry and lithology of a glacier valley) are future modeling targets. Regional climate can also vary out of phase with the marine isotope record; any long-term drift in climate associated with changes in atmospheric circulation could alter the pattern of moraine positions expected solely from Plio-Pleistocene vertical erosion (e.g., Krinner et al., 2011).

The magnitude of the erosional feedback we illustrate is sufficient to explain the observed reduction in glacier length from the maximum glacier extent, at least in those sites in which the reduction is of the order of several tens of percent (see Fig. 2B), without appealing to a drift in the intensity and variability of glacial climates through the Quaternary. Given that the million-year drift in climate (e.g., Fig. 1A) has been toward more, rather than less, intense glacials, preservation of ancient moraines in fact requires that some effect counters this climate drift, as pointed out by Kaplan et al. (2009). The erosional feedback described above supports this notion. For those sites in which the reduction in glacier length is greater, one may need to appeal to

other processes, such as drift in regional climate or blockage of moisture sources, that work in concert with the erosional feedback to reduce glacier health.

The robust nature of the analysis makes it tempting to invert the landscape evolution problem. For example, can we answer the question: how much erosion must have occurred in a glacial valley to produce an observed reduction in moraine length? We expect that such an analysis is best suited for cases in which non-erosional effects can be excluded and moraines of known and significantly different age were employed. Any such analysis, however, would be subject to error associated with discrepancies between real and prescribed climates, including accurate reproduction of local climate variability between glaciations. Precise, site-specific climate histories over the Plio-Pleistocene remain elusive. However, the recent development of transient GCMs and improved downscaling techniques may help constrain local climate conditions over glacial – interglacial cycles (Liu et al., 2009).

Any significant motion of a mountain range will alter the climate experienced by the landscape carved into it. Erosion induces an inevitable isostatic response to the unloading that raises both the valley floor and the ridges and peaks above it. Our work echoes the analysis in Small and Anderson (1998), who demonstrated that the effect is relatively minor in the case of alpine valleys. Isostatic rock uplift, on the order of a few meters over 1 My, is illustrated by differences between initial and final bedrock profiles onboard of the glacial extents in simulations in which tectonically induced rock uplift is negligible (e.g., Figs. 13, 16 and 18A). Given the reasonable effective elastic thickness of several tens of kilometers (in our models, 25 km), the isostatic response to the erosion of a few hundred meters in a valley 20 km long and spaced by several kilometers from any adjacent valley will be spread over several hundred kilometers. The isostatic response is small locally because the flexural wavelength is long relative to glacial valleys and because glaciers occupy only a fraction of the mountain landscape.

Our modeling suggests that while the erosional feedback on glacier length depends upon the mean erosion of the valley, the type of climatic driver strongly influences the magnitude and pattern of glacial erosion. Regions in which glacial histories are primarily governed by variations in the amount of snowfall (winter balance driven) generally experience higher glacial erosion rates compared to a region in which glacier histories are primarily governed by air temperature (cf. Figs. 13 and 16). This reflects the evolution of the thermal state at the glacier bed: in winter balance-dominated glaciers, the bed remains at the PMP and sliding is allowed in the accumulation zone; in air temperature-dominated glaciers, the bed at high elevations in the accumulation zone can remain below the PMP and is hence frozen to the bed, which in turn prevents sliding-induced erosion. These results suggest that the magnitude of glacier erosion may be smaller in thermally modulated cases. Detailed inspection of the initial and final profiles in these cases (Figs. 13 and 16) reveals the contrast in erosional response: 150 m of erosion occurs at 3700 m elevation in the b_w -dominated case, while erosion is negligible at this elevation in the thermally modulated case. Large portions of glacial valleys and their associated headwalls can thereby escape erosion under thermally modulated conditions. The logical extrapolation of this effect in tectonically active ranges would be the generation of very high, untouchable portions of the landscape that have escaped the 'glacial buzzsaw', as discussed in Ward et al. (2012). While we acknowledge that cases in which mountain peaks protude exceptionally high above the ELA are rare, our results show that the thermal state of a glacier can potentially exert considerable control on the magnitude and spatial pattern of long-term glacial erosion in alpine valleys. Therefore, when assessing the combined influences of glacial erosion, lithology, and rock uplift/subsidence in landscape evolution, it is important to consider whether a mountain range exists in a location where glaciers are modulated by winter balance or summer balance.

7. Conclusions

Far-flung moraines are quite common. In many cases the older moraines are many kilometers beyond the LGM moraines. On the other hand, inspection of the global marine isotope record, taken as a proxy for variations in the magnitude of global ice volume over the last five million years, suggests that the LGM was comparable to the largest ice volume (and hence extent) over this period. Reconciliation of these observations requires a mechanism that can produce long-term drift toward smaller glacier lengths, despite the roughly equal magnitudes of glacial climates.

We explored one mechanism that appears to be capable of quantitatively explaining the long-term drift in the glacial response of a landscape to the Quaternary climate swings. Our analytical results and numerical models show that far-flung moraines are an inevitable consequence of glacial erosion at all sites where erosion outpaces rock uplift. The simple analytical treatment suggests that the reduction in glacier length, when normalized by the maximum glacier extent, should reflect the cumulative erosion when scaled against the elevation range of the accumulation area. Due to this downward migration of the bed profile, in subsequent glaciations, a given alpine glacier will experience a lower mean elevation and, therefore, a smaller accumulation area.

The numerical modeling experiments bear this out. The results are robust against the details of the glacier model and the climate forcing. Air temperature (modulating summer balance) and snowfall (modulating winter balance) driven glaciers produce sets of moraines that decline in length. In all cases, the reduction in glacier length is well predicted by the mean erosion of the bed. The insensitivity to climate forcing and to the details of glacier hydrology, sliding, and erosion processes implies that the mean lowering of the bed profile is the dominant control of glacier erosion-length feedback.

The details matter, however, in governing the detailed geometry of the resulting glacially modified valley. The thermal component of the numerical model has allowed us to illustrate how the high elevations of a glacial valley can become immune to erosion and thereby escape the glacial buzz-saw. When coupled with strong rock that is both difficult to erode and can maintain tall walls, this effect may promote the evolution of very high mountains (Ward et al., 2012).

This glacier erosion-length feedback can be countered by surface uplift. In places where surface uplift exceeds the mean rate of erosional lowering, such as the leading edge of Yellowstone Hotspot, glacier lengths at glacial maxima should increase over time and eliminate old moraines. On the other hand, glacial valleys experiencing rock subsidence, such as the trailing edge of Yellowstone Hotspot, or in Hawaii, should experience faster rates of decline in glacier length, resulting in preservation of a larger number of moraines.

Acknowledgments

We gratefully acknowledge funding from the National Science Foundation (to R.S. Anderson and M. Dühnforth: EAR-0922126; to R.S. Anderson: EAR-1123855; and to the Boulder Creek CZO: EAR-0724960). L. Anderson acknowledges support through an NSF graduate fellowship. We appreciate the insightful and thorough reviews of Drs. Kaplan and Schomacker, and the attention to detail shown by Editor R. Marston.

References

- Anderson, R.S., Anderson, S.P., MacGregor, K.R., O'Neel, S., Riihimaki, C.A., Waddington, E.D., Loso, M.G., 2004. Strong feedbacks between hydrology and sliding of a small alpine glacier. *Journal of Geophysical Research*, Earth Surface 109, F1. <http://dx.doi.org/10.1029/2004JF000120>.
- Anderson, R.S., Molnar, P., Kessler, M.A., 2006. Features of glacial valley profiles simply explained. *Journal of Geophysical Research* 111, F01004. <http://dx.doi.org/10.1029/2005JF000344>.
- Anslow, F.S., Hostetler, S., Bidlake, W.R., Clark, P.U., 2008. Distributed energy balance modeling of South Cascade Glacier, Washington and assessment of model uncertainty. *Journal of Geophysical Research* 113, F02019. <http://dx.doi.org/10.1029/2007JF000850>.
- Bahr, D., Rundle, J., 1995. Theory of lattice Boltzmann simulations of glacier flow. *Journal of Glaciology* 41, 634–640.
- Bartholomaeus, T.C., Anderson, R.S., Anderson, S.P., 2007. Response of glacial basal motion to transient water storage. *Nature Geoscience* 1 (1), 33–37. <http://dx.doi.org/10.1038/ngeo.2007.5298>.
- Bierman, P., Gillespie, A., Whipple, K., Clark, D., 1991. Quaternary geomorphology and geochronology of Owens Valley, California. *Geological Excursions in Southern California and Mexico: In: Walawender, M.J., Hahan, B.B. (Eds.), Guidebook for the 1991 Annual Meeting, Geological Society of America*, pp. 199–223.
- Birkeland, P.W., 1964. Pleistocene glaciation of the northern Sierra Nevada, north of Lake Tahoe, California. *Journal of Geology* 72, 810–825.
- Birman, J.H., 1964. Glacial geology across the crest of the Sierra Nevada, California. *Geological Society of America Special Paper* 75, 1–80.
- Blackwelder, E., 1915. Post-Cretaceous history of the mountains of central western Wyoming. *Journal of Geology* 23, 97–117, 193–217, 307–340.
- Blackwelder, E., 1929. Moraines of Convict Lake glaciers. *Geological Society of America Abstracts and Program* 40, 171.
- Blackwelder, E., 1931. Pleistocene glaciation in the Sierra Nevada and Basin Ranges. *Geological Society of America Bulletin* 42, 865–922.
- Braithwaite, R.J., Olesen, O.B., 1989. Calculation of glacier ablation from air temperature, West Greenland. In: Oerlemans, J. (Ed.), *Glacier Fluctuations and Climatic Change*. Kluwer Academic, Dordrecht, The Netherlands, pp. 219–233.
- Brocklehurst, S.H., Whipple, K.X., 2002. Glacial erosion and relief production in the eastern Sierra Nevada, California. *Geomorphology* 42, 1–24.
- Brook, E.J., Kurz, M.D., Ackert, R.P., Denton, G.H., Brown, E.T., Raisbeck, G.M., Yiou, F., 1993. Chronology of Taylor Glacier advances in Arena Valley, Antarctica, using in situ cosmogenic ^3He and ^{10}Be . *Quaternary Research* 39, 11–23.
- Colgan, P.M., Munroe, J.S., Shangzhe, Z., 2006. Cosmogenic radionuclide evidence for the limited extent of Last Glacial Maximum glaciers in the Tanggula Shan of the central Tibetan Plateau. *Quaternary Research* 65 (2), 336–339.
- Colgan, W., Zwally, H., Abdalati, W., Joughin, I., Anderson, R.S., Steffen, K., Rajaram, H., Phillips, T., 2011. The annual glaciohydrology cycle in the ablation zone of the Greenland Ice Sheet: part 1. Hydrology model. *Journal of Glaciology* 57 (204), 697–709.
- Colgan, W., Rajaram, H., Anderson, R.S., Steffen, K., Phillips, T., Abdalati, W., 2012. The annual glaciohydrology cycle in the ablation zone of the Greenland Ice Sheet: part 2. Ice flow model. *Journal of Glaciology* 58, 51–64.
- Colhoun, E.A., Barrows, T.T., 2011. The glaciation of Australia. *Quaternary Glaciations – Extent and Chronology: A Closer Look, Part 4. Elsevier, Amsterdam, The Netherlands*, pp. 1037–1046.
- Crowley, J.L., Schoene, B., Bowring, S.A., 2007. U–Pb dating of zircon in the Bishop Tuff at the millennial scale. *Geology* 35 (12), 1123–1126.
- Curry, R., 1971. Glacial and Pleistocene history of the Mammoth Lakes Sierra: A geologic guidebook prepared in conjunction with the Sept. 11–12, 1971. Field Conference of the Pacific Coast Division, Friends of the Pleistocene, University of Montana Department of Geology, Missoula, MT, pp. 1–49.
- Dahms, D.E., 2004. Relative and numeric age data for Pleistocene glacial deposits and diamictites in and near Sinks Canyon, Wind River Range, Wyoming, USA. *Arctic, Antarctic, and Alpine Research* 36 (1), 59–77.
- Dethier, D.P., Benedict, J.B., Birkeland, P.W., Caine, N., Davis, P.T., Madole, R.F., Patterson, P.E., Price, A.B., Schildgen, T.F., Shroba, R.R., 2003. Quaternary stratigraphy, geomorphology, soils, and alpine archaeology in an alpine-to-plains transect, Colorado Front Range. In: Easterbrook, D.J. (Ed.), *Quaternary Geology of the United States: INQUA 2003 field guide volume, XVI INQUA Congress, Desert Research Institute, Reno, NV*, pp. 81–104.
- DiBiase, R.A., Whipple, K.X., Heimsath, A.M., Ouimet, W.B., 2010. Landscape form and millennial erosion rates in the San Gabriel Mountains, CA. *Earth and Planetary Science Letters* 289, 134–144.
- Dühnforth, M., Anderson, R.S., 2011. Reconstructing the glacial history of Green Lakes Valley, North Boulder Creek, Front Range, Colorado, using ^{10}Be exposure dating. *Arctic Alpine Antarctic Research* 3 (4), 527–542.
- Duk-Rodkin, A., 1999. Glacial limits map of Yukon Territory. *Geological Survey of Canada, Open File* 3694, Yukon Geology Program, Plate 1.
- Duk-Rodkin, A., Barendregt, R., Froese, D., Weber, F., Enkin, R., Rodsmith, I., Zazula, G., Waters, P., Klassen, R., 2004. Timing and extent of Plio-Pleistocene glaciations in Northwestern Canada and East-Central Alaska. In: Ehlers, J., Gibbard, P.L. (Eds.), *Quaternary Glaciations – Extent and Chronology Part II: North America, Developments in Quaternary Science* 2. Elsevier, Amsterdam, The Netherlands, pp. 313–335.
- Fitzsimons, S.J., Colhoun, E.A., 1991. Pleistocene glaciation of the King Valley, western Tasmania, Australia. *Quaternary Research* 36 (2), 135–156.
- Funk, M., Echelmeyer, K., Iken, A., 1994. Mechanisms of fast flow in Jakobshavn Isbrae, West Greenland: part II. Modeling of englacial temperatures. *Journal of Glaciology* 40, 569–585.
- Fushimi, H., 1978. Glaciations in the Khumbu Himal. *Journal of the Japanese Society of Snow and Ice* 40, 71–77.
- Gibbons, A.B., Megeath, J.D., Pierce, K.L., 1984. Probability of moraine survival in a succession of glacial advances. *Geology* 12, 327–330.
- Glen, J.W., 1955. The creep of polycrystalline ice. *Proceedings of the Royal Society of London. Series A: Mathematical and Physical Sciences* 228, 519–538.
- Glen, J.W., 1958. The flow law of ice. A discussion of the assumptions made in glacier theory, their experimental foundations and consequences. *International Association of Scientific Hydrology* 47, 171–183.
- Hallet, B., Hunter, L., Bogen, J., 1996. Rates of erosion and sediment evacuation by glaciers: a review of field data and their implications. *Global and Planetary Change* 12, 213–235.

- Hamilton, T.D., 1986. Late Cenozoic glaciation of the central Brooks Range. In: Hamilton, T.D., Reed, K.M., Thorson, R.M. (Eds.), *Glaciation in Alaska—The Geologic Record*. Alaska Geological Society, Anchorage, pp. 9–49.
- Hamilton, T.D., 1994. Late Cenozoic glaciation of Alaska. In: Pflafer, G., Berg, H.C. (Eds.), *The Geology of Alaska*, Geological Society of America, Boulder, CO, The Geology of North America G-1, pp. 813–844.
- Hedrick, K., Seong, Y.B., Owen, L.A., Caffee, M.W., Dietsch, C., 2011. Towards defining the transition in style and timing of Quaternary glaciation between the monsoon-influenced Greater Himalaya and the semi-arid Trans-Himalaya of northern India. *Quaternary International* 236 (1–2), 21–33.
- Hock, R., 2003. Temperature index melt modelling in mountain areas. *Journal of Hydrology* 282, 104–115.
- Hooke, R. LeB., 2005. *Principles of Glacier Mechanics*, 2nd ed. Cambridge University Press, Cambridge, UK, 429 pp.
- Hughes, P.D., Woodward, J.C., Gibbord, P.L., Macklin, M.G., Gilmour, M.A., Smith, G.R., 2006. The glacial history of the Pindus Mountains, Greece. *Journal of Geology* 114 (4), 413–433.
- Humphrey, N.F., Raymond, C.F., 1994. Hydrology, erosion and sediment production in a surging glacier: Variegated Glacier, Alaska, 1982–83. *Journal of Glaciology* 40, 539–552.
- Huybers, P., 2006. Early Pleistocene glacial cycles and the integrated summer insolation forcing. *Science* 313, 508–511.
- Jóhannesson, T., Raymond, C., Waddington, E., 1989. Time scale for adjustment of glaciers to changes in mass balance. *Journal of Glaciology* 35, 355–369.
- Johnson, W.D., 1904. The profile of maturity in alpine glacial erosion. *Journal of Geology* 12, 569–578.
- Kaplan, M.R., Douglass, D.C., Singer, B.S., Ackert, R.P., Caffee, M.W., 2005. Cosmogenic nuclide chronology of pre-last glacial maximum moraines at Lago Buenos Aires, 46°S, Argentina. *Quaternary Research* 63 (3), 301–315.
- Kaplan, M.R., Hein, A.S., Hubbard, A., Lax, S.M., 2009. Can glacial erosion limit the extent of glaciation? *Geomorphology* 103, 72–79.
- Karlstrom, E.T., 2000. Fabric and origin of multiple diamictites within the pre-Illinoian Kennedy drift east of Waterton-Glacier International Peace Park, Alberta, Canada, and Montana, USA. *Geological Society of America Bulletin* 112 (10), 1496–1506.
- Kaufman, D.S., Hopkins, D.M., 1986. Glacial history of the Seward Peninsula. In: Hamilton, T.D., Reed, K.M., Thorson, R.M. (Eds.), *Glaciation in Alaska—The Geologic Record*. Alaska Geological Society, Anchorage, pp. 51–77.
- Kessler, M.A., Anderson, R.S., 2004. Testing a numerical glacial hydrological model using spring speed-up events and outburst floods. *Geophysical Research Letters* 31 (L18503). <http://dx.doi.org/10.1029/2004GL020622>.
- Kessler, M.A., Anderson, R.S., Stock, G.S., 2006. Modeling topographic and climatic control of east–west asymmetry in Sierra Nevada glacier length during the Last Glacial Maximum. *Journal of Geophysical Research* 111 (F2), F02002. <http://dx.doi.org/10.1029/2005JF003365>.
- Kline, J.T., Bundtzen, T.K., 1986. Two glacial records from west-central Alaska. In: Hamilton, T.D., Reed, K.M., Thorson, R.M. (Eds.), *Glaciation in Alaska—The Geologic Record*. Alaska Geological Society, Anchorage, pp. 123–150.
- Krinner, G., Diekmann, B., Colleoni, F., Stauch, G., 2011. Global, regional and local scale factors determining glaciation extent in eastern Siberia over the last 140,000 years. *Quaternary Science Reviews* 30 (7–8), 821–831.
- Lehmkuhl, F., 1998. Extent and spatial distribution of Pleistocene glaciations in eastern Tibet. *Quaternary International* 45 (1), 123–134.
- Lisiecki, L.E., Raymo, M.E., 2005. A Pliocene–Pleistocene stack of 57 globally distributed benthic $\delta^{18}\text{O}$ records. *Paleoceanography* 20, PA1003.
- Liu, Z., Otto-Bliesner, B.L., He, F., Brady, E.C., Tomas, R., Clark, P.U., Carlson, A.E., Lynch-Stieglitz, J., Curry, W., Brook, E., Erickson, D., Jacob, R., Kutzbach, J., Cheng, J., 2009. Transient simulation of last deglaciation with a new mechanism for Bolling–Allerød warming. *Science* 325 (5938), 310–314.
- MacGregor, K.R., Anderson, R.S., Anderson, S.P., Waddington, E.D., 2000. Numerical simulations of glacial-valley longitudinal profile evolution. *Geology* 28, 1031–1034.
- MacGregor, K.R., Anderson, R.S., Waddington, E.D., 2009. Numerical modeling of glacial erosion and headwall processes in alpine valleys. *Geomorphology* 103, 189–204. <http://dx.doi.org/10.1016/j.geomorph.2008.04.022>.
- Marshall, S.J., Björnsson, H., Flowers, G.E., Clarke, G.K.C., 2005. Simulation of Vatnajökull ice cap dynamics. *Journal of Geophysical Research* 110, F03009.
- Nishiizumi, K., Winterer, E.L., Kohl, C.P., Klein, J., Middleton, R., Lal, D., Arnold, J.R., 1989. Cosmic ray production rates of ^{10}Be and ^{26}Al in quartz from glacially polished rocks. *Journal of Geophysical Research* 94, 17,907–17,915.
- Oerlemans, J., 1984. Numerical experiments on large-scale glacial erosion. *Zeitschrift für Gletscherkunde und Glazialgeologie* 20, 107–126.
- Ohmura, A., 2001. Physical basis for the temperature-based melt-index method. *Journal of Applied Meteorology* 40, 753–761.
- Owen, L., Finkel, R., Barnard, P., Haizhou, M., Asahi, K., Caffee, M., Derbyshire, E., 2005. Climatic and topographic controls on the style and timing of late Quaternary glaciation throughout Tibet and the Himalaya defined by Be cosmogenic radionuclide surface exposure dating. *Quaternary Science Reviews* 24 (12–13), 1391–1411.
- Owen, L.A., Caffee, M.W., Bovard, K.R., Finkel, R.C., Sharma, M.C., 2006. Terrestrial cosmogenic nuclide surface exposure dating of the oldest glacial successions in the Himalayan orogen: Ladakh Range, northern India. *Geological Society of America Bulletin* 118 (3–4), 383–392.
- Owen, L.A., Yi, C., Finkel, R.C., Davis, N.K., 2010. Quaternary glaciation of Gurla Mandhata (Naimon'anyi). *Quaternary Science Reviews* 29 (15–16), 1817–1830.
- Pfeffer, W.T., Meier, M.F., Illangasekare, T.H., 1991. Retention of Greenland runoff by refreezing: implications for projected future sea level change. *Journal of Geophysical Research* 96 (C12), 22,117–22,124. <http://dx.doi.org/10.1029/91JC02502>.
- Phillips, F.M., McIntosh, W.C., Dunbar, N.W., 2011. Chronology of late Cenozoic volcanic eruptions onto relic surfaces in the south-central Sierra Nevada, California. *Geological Society of America Bulletin*. <http://dx.doi.org/10.1130/B30000.1>.
- Pierce, K.L., 2003. Pleistocene glaciations of the Rocky Mountains. The Quaternary Period in the United States. In: Gillespie, A.R., Porter, S.C., Atwater, B.F. (Eds.), *Developments in Quaternary Science*, 1. Elsevier, pp. 63–76.
- Pierce, K.L., Morgan, L.A., 1992. The track of the Yellowstone hot spot: volcanism, faulting, and uplift. *Regional Geology of Eastern Idaho and Western Wyoming*. In: Link, P.K., Kuntz, M.A., Platt, L.B. (Eds.), *Geological Society of America Memoir*, Geological Society of America, Boulder, CO, 179, pp. 1–52.
- Porter, S.C., 1976. Pleistocene glaciation in the southern part of the North Cascade Range, Washington. *Geological Society of America Bulletin* 87 (1), 61–75.
- Porter, S.C., 1979. Hawaiian glacial ages. *Quaternary Research* 12 (2), 161–187.
- Porter, S.C., 1989. Some geological implications of average Quaternary glacial conditions. *Quaternary Research* 32, 245–261.
- Reillinger, R.E., 1985. Vertical movements associated with the 1959, $M=7.1$ Hebgen Lake Montana earthquake. *Proceedings, Workshop XXVIII on the Borah Peak, Idaho, Earthquake*. In: Stein, R.S., Bucknam, R.C. (Eds.), *U.S. Geological Survey Open-File Report 85–290*, Menlo Park, CA, pp. 519–530.
- Roe, G.H., 2011. What do glaciers tell us about climate? *Journal of Glaciology* 57 (203), 567–578.
- Roe, G.H., O'Neal, M.A., 2009. The response of glaciers to intrinsic climate variability: observations and models of late-Holocene variations in the Pacific Northwest. *Journal of Glaciology* 55 (193), 839–854.
- Russell, I.C., 1889. Quaternary history of Mono Valley, California. USGS 8th Annual Report 1, Washington, DC, pp. 261–394.
- Saunders, A.D., Jones, S.M., Morgan, L.A., Pierce, K.L., Widdowson, M., Xu, Y.G., 2007. Regional uplift associated with continental large igneous provinces: the roles of mantle plumes and the lithosphere. *Chemical Geology* 241 (3–4), 282–318.
- Schmoll, H.R., Yehle, L.A., 1986. Pleistocene glaciation of the upper Cook Inlet Basin. In: Hamilton, T.D., Reed, K.M., Thorson, R.M. (Eds.), *Glaciation in Alaska—The Geologic Record*. Alaska Geological Society, Anchorage, pp. 193–218.
- Sharp, R.P., 1968. Sherwin till-Bishop tuff geological relationships, Sierra Nevada, California. *Geological Society of America Bulletin* 79, 351–364.
- Sharp, R.P., 1972. Pleistocene glaciation, Bridgeport basin, California. *Geological Society of America Bulletin* 83 (8), 2233–2268.
- Singer, B.S., Ackert, R.P., Guillou, H., 2004. $^{40}\text{Ar}/^{39}\text{Ar}$ and K–Ar chronology of Pleistocene glaciations in Patagonia. *Geological Society of America Bulletin* 116 (3), 434–450.
- Small, E.E., Anderson, R.S., 1998. Pleistocene relief production in Laramide mountain ranges, western United States. *Geology* 26, 123–126.
- Smith, J.A., Finkel, R.C., Farber, D.L., Rodbell, D.T., Seltzer, G.O., 2005. Moraine preservation and boulder erosion in the tropical Andes: interpreting old surface exposure ages in glaciated valleys. *Journal of Quaternary Science* 20 (7–8), 735–758.
- Stauch, G., Gualtieri, L., 2008. Late Quaternary glaciations in northeastern Russia. *Journal of Quaternary Science* 23, 545–558.
- Suggate, R.P., 1990. Late Pliocene and Quaternary glaciations of New Zealand. *Quaternary Geochronology* 9 (2), 175–197.
- Thorson, R.M., 1986. Late Cenozoic glaciation of the northern Nenana River valley. In: Hamilton, T.D., Reed, K.M., Thorson, R.M. (Eds.), *Glaciation in Alaska—The Geologic Record*. Alaska Geological Society, Anchorage, pp. 171–191.
- VanderVeen, C., 1987. Longitudinal stresses and basal sliding: a comparative study. In: VanderVeen, C., Oerlemans, J. (Eds.), *Dynamics of the West Antarctic Ice Sheet*. D. Reidel, Dordrecht, pp. 223–248.
- van Husan, D., 2004. Quaternary glaciations in Austria. In: Ehlers, J., Gibbard, P.L. (Eds.), *Quaternary Glaciations Extent and Chronology Part I: Europe*, *Developments in Quaternary Science* 2. Elsevier, Amsterdam, The Netherlands, pp. 1–13.
- Wang, J., Zhou, S., Tang, S., Colgan, P.M., Munroe, J.S., 2007. The sequence of Quaternary glaciations around Tanggula Pass. *Journal of Glaciology and Geocryology* 29, 149–155 (in Chinese).
- Ward, D.J., Anderson, R.S., Haeussler, P.J., 2012. Scaling the Teflon peaks: granite, glaciers, and the highest relief in North America. *JGR–Earth Surface* 117 (F01023). <http://dx.doi.org/10.1029/2011JF002068>.
- Weber, F.R., 1986. Glacial geology of the Yukon-Tanana upland. In: Hamilton, T.D., Reed, K.M., Thorson, R.M. (Eds.), *Glaciation in Alaska—The Geologic Record*. Alaska Geological Society, Anchorage, AK, pp. 79–98.
- Weber, F.R., Hamilton, T.D., 1982. *Glacial Geology of the Mt. Prindel Area, Yukon-Tanana Upland, Alaska*. Professional Report 86, Alaska Division of Geological and Geophysical Surveys, Fairbanks, AK, pp. 42–48.
- Whipple, K.X., 2004. Bedrock rivers and the geomorphology of active orogens. *Annual Reviews of Earth and Planetary Science* 32, 151–185.
- Xu, L., Zhou, S., 2009. Quaternary glaciations recorded by glacial and fluvial landforms in the Shaluli Mountains, southeastern Tibetan Plateau. *Geomorphology* 103 (2), 268–275.
- Yi, C., Li, X., Qu, J., 2002. Quaternary glaciation of Puruogangri – the largest modern ice field in Tibet. *Quaternary International* 98, 111–121.